arXiv:0807.3834v1 [hep-ex] 24 Jul 2008

Exclusive ρ^0 electroproduction on the proton at CLAS

S.A. Morrow[1,2], M. Guidal[1a], M. Garçon[2], J.M. Laget[2,3], E.S. Smith[3], G. Adams[4], K.P. Adhikari[5], M. Aghasyan[6], M.J. Amaryan[5], M. Anghinolfi[7], G. Asryan[8], G. Audit[2], H. Avakian[3], H. Bagdasaryan[8,5], N. Baillie[9], J.P. Ball[10], N.A. Baltzell[11], S. Barrow[12], M. Battaglieri[7], I. Bedlinskiy[13], M. Bektasoglu[14,5], M. Bellis[15], N. Benmouna[16], B.L. Berman[16], A.S. Biselli[17], L. Blaszczyk[18], B.E. Bonner[19], C. Bookwalter[18], S. Bouchigny[1], S. Boiarinov[13,3], R. Bradford[15], D. Branford[20], W.J. Briscoe[16], W.K. Brooks[3,21], S. Bültmann[5], V.D. Burkert[3], C. Butuceanu[9], J.R. Calarco[22], S.L. Careccia[5], D.S. Carman[3], B. Carnahan[23], L. Casey[23], A. Cazes[11], S. Chen[18], L. Cheng[23], P.L. Cole[3,24], P. Collins[10], P. Coltharp[12], D. Cords[3], P. Corvisiero[7], D. Crabb[25], H. Crannell[23], V. Crede[18], J.P. Cummings[4], D. Dale[24], N. Dashyan[8], R. De Masi[1,2], R. De Vita[7], E. De Sanctis[6], P.V. Degtyarenko[3], H. Denizli[26], L. Dennis[18], A. Deur[3], S. Dhamija[27], K.V. Dharmawardane[5], K.S. Dhuga[16], R. Dickson[15], J.-P. Didelez[1], C. Djalali[11], G.E. Dodge[5], D. Doughty[28], M. Dugger[10], S. Dytman[26], O.P. Dzyubak[11], H. Egiyan[22,9,3], K.S. Egiyan[8], L. El Fassi[29], L. Elouadrhiri[3], P. Eugenio[18], R. Fatemi[25], G. Fedotov[30], R. Fersch[9], R.J. Feuerbach[15], T.A. Forest[24], A. Fradi[1], G. Gavalian[22,5], N. Gevorgyan[8], G.P. Gilfoyle[31], K.L. Giovanetti[32], F.X. Girod[3,2], J.T. Goetz[33], W. Gohn[34], C.I.O. Gordon[35], R.W. Gothe[11], L. Graham[11], K.A. Griffioen[9], M. Guillo[11], N. Guler[5], L. Guo[3], V. Gyurjyan[3], C. Hadjidakis[1], K. Hafidi[29], H. Hakobyan[8], C. Hanretty[18], J. Hardie[28,3], N. Hassall[35], D. Heddle[28,3], F.W. Hersman[22], K. Hicks[14], I. Hleiqawi[14], M. Holtrop[22], E. Hourany[1], C.E. Hyde-Wright[5], Y. Ilieva[16], D.G. Ireland[35], B.S. Ishkhanov[30], E.L. Isupov[30], M.M. Ito[3], D. Jenkins[36], H.S. Jo[1], J.R. Johnstone[35], K. Joo[34,3], H.G. Juengst[5], N. Kalantarians[5], D. Keller[14], J.D. Kellie[35], M. Khandaker[37], P. Khetarpal[4], W. Kim[38], A. Klein[5], F.J. Klein[23], A.V. Klimenko[5], M. Kossov[13], L.H. Kramer[27,3], V. Kubarovsky[3], J. Kuhn[4,15], S.E. Kuhn[5], S.V. Kuleshov[13,21], V. Kuznetsov[38], J. Lachniet[15,5], J. Langheinrich[11], D. Lawrence[39], Ji Li[4], K. Livingston[35], H.Y. Lu[11], M. MacCormick[1], C. Marchand[2], N. Markov[34], P. Mattione[19], S. McAleer[18], M. McCracken[15], B. McKinnon[35], J.W.C. McNabb[15], B.A. Mecking[3], S. Mehrabyan[26], J.J. Melone[35], M.D. Mestayer[3], C.A. Meyer[15], T. Mibe[14], K. Mikhailov[13], R. Minehart[25], M. Mirazita[6], R. Miskimen[39], V. Mokeev[30,3], L. Morand[2], B. Moreno[1], K. Moriya[15], M. Moteabbed[27], J. Mueller[26], E. Munevar[16], G.S. Mutchler[19], P. Nadel-Turonski[16], R. Nasseripour[16,27,11], S. Niccolai[1], G. Niculescu[32,14], I. Niculescu[32,16,3], B.B. Niczyporuk[3], M.R. Niroula[5], R.A. Niyazov[4,5], M. Nozar[3], G.V. O'Rielly[16], M. Osipenko[7,30], A.I. Ostrovidov[12], K. Park[38,11], S. Park[18], E. Pasyuk[10], C. Paterson[35], S. Anefalos Pereira[6], S.A. Philips[16], J. Pierce[25], N. Pivnyuk[13], D. Pocanic[25], O. Pogorelko[13], E. Polli[6], I. Popa[16], S. Pozdniakov[13], B.M. Preedom[11], J.W. Price[40], S. Procureur[2], Y. Prok[25,28,3], D. Protopopescu[22,35], L.M. Qin[5], B.A. Raue[27,3], G. Riccardi[18], G. Ricco[7], M. Ripani[7], B.G. Ritchie[10], G. Rosner[35], P. Rossi[6], P.D. Rubin[31], F. Sabatié[2], M.S. Saini[18], J. Salamanca[24], C. Salgado[37], J.P. Santoro[23], V. Sapunenko[3], D. Schott[27], R.A. Schumacher[15], V.S. Serov[13], Y.G. Sharabian[3], D. Sharov[30], N.V. Shvedunov[30], A.V. Skabelin[41], L.C. Smith[25], D.I. Sober[23], D. Sokhan[20], A. Stavinsky[13], S.S. Stepanyan[38], S. Stepanyan[3], B.E. Stokes[18], P. Stoler[4], I.I. Strakovsky[16], S. Strauch[11,16], M. Taiuti[7], D.J. Tedeschi[11], A. Tkabladze[14,16], S. Tkachenko[5], L. Todor[31,15], C. Tur[11], M. Ungaro[34,4], M.F. Vineyard[42,31], A.V. Vlassov[13], D.P. Watts[20,35], L.B. Weinstein[5], D.P. Weygand[3], M. Williams[15], E. Wolin[3], M.H. Wood[11], A. Yegneswaran[3], M. Yurov[38], L. Zana[22], J. Zhang[5], B. Zhao[34], and Z.W. Zhao[11]

(CLAS Collaboration)

[1] Institut de Physique Nucleaire ORSAY, Orsay, France
[2] CEA-Saclay, Service de Physique Nucléaire, 91191 Gif-sur-Yvette, France
[3] Thomas Jefferson National Accelerator Facility, Newport News, Virginia 23606
[4] Rensselaer Polytechnic Institute, Troy, New York 12180-3590
[5] Old Dominion University, Norfolk, Virginia 23529
[6] INFN, Laboratori Nazionali di Frascati, 00044 Frascati, Italy
[7] INFN, Sezione di Genova, 16146 Genova, Italy
[8] Yerevan Physics Institute, 375036 Yerevan, Armenia
[9] College of William and Mary, Williamsburg, Virginia 23187-8795
[10] Arizona State University, Tempe, Arizona 85287-1504
[11] University of South Carolina, Columbia, South Carolina 29208
[12] Florida State University, Tallahassee, Florida 32306

[a] *Corresponding author:* guidal@ipno.in2p3.fr

2

[13] Institute of Theoretical and Experimental Physics, Moscow, 117259, Russia
[14] Ohio University, Athens, Ohio 45701
[15] Carnegie Mellon University, Pittsburgh, Pennsylvania 15213
[16] The George Washington University, Washington, DC 20052
[17] Fairfield University, Fairfield CT 06824
[18] Florida State University, Tallahassee, Florida 32306
[19] Rice University, Houston, Texas 77005-1892
[20] Edinburgh University, Edinburgh EH9 3JZ, United Kingdom
[21] Universidad Técnica Federico Santa María, Casilla 110-V, Valparaíso, Chile
[22] University of New Hampshire, Durham, New Hampshire 03824-3568
[23] Catholic University of America, Washington, D.C. 20064
[24] Idaho State University, Pocatello, Idaho 83209
[25] University of Virginia, Charlottesville, Virginia 22901
[26] University of Pittsburgh, Pittsburgh, Pennsylvania 15260
[27] Florida International University, Miami, Florida 33199
[28] Christopher Newport University, Newport News, Virginia 23606
[29] Argonne National Laboratory, Illinois 60439
[30] Moscow State University, General Nuclear Physics Institute, 119899 Moscow, Russia
[31] University of Richmond, Richmond, Virginia 23173
[32] James Madison University, Harrisonburg, Virginia 22807
[33] University of California at Los Angeles, Los Angeles, California 90095-1547
[34] University of Connecticut, Storrs, Connecticut 06269
[35] University of Glasgow, Glasgow G12 8QQ, United Kingdom
[36] Virginia Polytechnic Institute and State University, Blacksburg, Virginia 24061-0435
[37] Norfolk State University, Norfolk, Virginia 23504
[38] Kyungpook National University, Daegu 702-701, Republic of Korea
[39] University of Massachusetts, Amherst, Massachusetts 01003
[40] California State University, Dominguez Hills, Carson, CA 90747
[41] Massachusetts Institute of Technology, Cambridge, Massachusetts 02139-4307
[42] Union College, Schenectady, NY 12308

Abstract. The $ep \to e'p\rho^0$ reaction has been measured, using the 5.754 GeV electron beam of Jefferson Lab and the CLAS detector. This represents the largest ever set of data for this reaction in the valence region. Integrated and differential cross sections are presented. The W, Q^2 and t dependences of the cross section are compared to theoretical calculations based on t-channel meson-exchange Regge theory on the one hand and on quark handbag diagrams related to Generalized Parton Distributions (GPDs) on the other hand. The Regge approach can describe at the $\approx 30\%$ level most of the features of the present data while the two GPD calculations that are presented in this article which succesfully reproduce the high energy data strongly underestimate the present data. The question is then raised whether this discrepancy originates from an incomplete or inexact way of modelling the GPDs or the associated hard scattering amplitude or whether the GPD formalism is simply inapplicable in this region due to higher-twists contributions, incalculable at present.

PACS. 13.60.Le Production of mesons by photons and leptons – 12.40.Nn Regge theory – 12.38.Bx Perturbative calculations

1 Introduction

The exclusive electroproduction of photons and mesons on the nucleon is an important tool to better understand nucleon structure and, more generally, the transition between the low energy hadronic and high energy partonic domains of the Quantum Chromodynamics (QCD) theory.

Among all such exclusive processes, the $ep \rightarrow e'p\rho^0$ reaction bears some particular advantages. It is a process for which numerical calculations and predictions are available both in terms of *hadronic* degrees of freedom, via Reggeized meson exchanges, and in terms of *partonic* degrees of freedom, via Generalized Parton Distributions

(GPDs). We refer the reader to refs. [1,2,3] and refs. [4, 5,6,7,8,9,10] for the original articles and general reviews of Regge theory and GPDs respectively. Defining Q^2 as the absolute value of the squared mass of the virtual photon that is exchanged between the electron and the target nucleon, partonic descriptions are expected to be valid at large Q^2, while hadronic descriptions dominate in photo- and low-Q^2 electroproduction. Fig. 1 illustrates these two approaches at the electron beam energies available at Jefferson Laboratory (JLab). Concerning the Reggeized meson exchange approach, the total and differential cross sections associated with the exchanges of the dominant

Regge σ and f_2 trajectories have been calculated by Laget *et al.* [11,12]. Concerning the GPDs approach, the so-called "handbag" diagram, with recent modelings of the unpolarized GPDs, has been calculated by two groups: Goloskokov-Kroll [13] and Vanderhaeghen *et al.* [14,15,16, 17]. Let us note here that in the GPD approach the leading twist handbag calculation is valid only for the longitudinal part of the cross section and that, experimentally, it is important to separate the longitudinal and transverse parts of the cross sections when measuring this process.
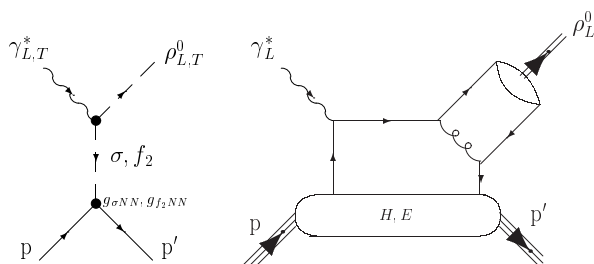
Fig. 1. The mechanisms for ρ^0 electroproduction at JLab energies for low Q^2 (left diagram) through the exchange of mesons and for high Q^2 (right diagram) through the quark exchange "handbag" mechanism (valid for longitudinal photons) where H and E are the unpolarized GPDs.

This article presents results for the exclusive electroproduction of the ρ^0 vector meson on the proton measured with the 5.754 GeV electron beam of the CEBAF accelerator and the CEBAF Large Acceptance Spectrometer (CLAS) at JLab. The aim of this analysis is to compare the integrated and differential cross sections of the $ep \rightarrow e'p\rho^0$ reaction that have been extracted over the intermediate Q^2 region accessible at CLAS, with the two Regge and GPD theoretical approaches, and thus determine their domain of validity and constrain their various inputs.

There are a few existing electroproduction data in a similar kinematical regime: early data with the 7.2 GeV beam at DESY [18] and with the 11.5 GeV beam at Cornell [19], and more recently with the 27 GeV beam at HERMES [20] and the 4.2 GeV beam of JLab [21]. The present work explores new phase-space regions and, in regions of overlap, has much finer binning and precision.

In section 2 we present the experimental procedure we have adopted to extract our integrated and differential cross sections. In section 3, after briefly describing the Regge and GPDs models, we compare these calculations to our data. Finally, we draw our conclusions in section 4.

2 Experimental procedure

The CLAS detector [22] is built around six superconduction coils that generate a toroidal magnetic field primarily in the azimuthal direction. Each sector is equipped with three regions of multi-wire drift chambers (DC) and time-of-flight scintillator counters (SC) that cover the angular range from 8° to 143°. In the forward region (8°< θ < 45°), each sector is furthermore equipped with a gas-filled threshold Cerenkov counter (CC) and a lead-scintillator sandwich type electromagnetic calorimeter (EC). Azimuthal coverage for CLAS is limited by the magnet's six coils and is approximatively 90% at large polar angles and 50% at forward angles.

The data were taken with an electron beam having an energy of 5.754 GeV impinging on an unpolarized 5-cm-long liquid-hydrogen target. The integrated luminosity of this data set was 28.5 fb^{-1}. The data were taken from October 2001 to January 2002. The kinematic domain of the selected sample corresponds approximately to Q^2 from 1.5 to 5.5 GeV^2. We analyzed data with W, the $\gamma^* - p$ center-of-mass energy, greater than 1.8 GeV, which corresponds to a range of x_B approximatively from 0.15 to 0.7. Here x_B is the standard Bjorken variable equal to $\frac{Q^2}{W^2-m_p^2+Q^2}$ with m_p the mass of the proton.

The ρ^0 decays into two pions ($\pi^+\pi^-$), with a branching ratio of 100% [23]. To select the channel $ep \rightarrow e'p\rho^0$, we based our analysis on the identification of the scattered electron, the recoil proton and the positive decay pion (because of the polarity of the magnetic field, negative pions are bent toward the beam pipe and in general escape the acceptance of CLAS); we then used the missing mass $ep \rightarrow e'p\pi^+X$ for the identification of the $ep \rightarrow e'p\pi^+\pi^-$ final state.

Once this final state is identified and its yield normalized, the reduced $\gamma^*p \rightarrow p\rho^0$ cross section is extracted by fitting in a model-dependent way the ($\pi^+\pi^-$) invariant mass using a parametrized ρ^0 shape, which will be described later. The longitudinal and transverse cross sections are then further extracted by analyzing the decay pion angular distribution in the ρ^0 center-of-mass frame. We detail all these steps in the following sections.

2.1 Particle identification

The electron is identified as a negative track, determined from the DC, having produced a signal in the CC and the EC. Pions, potentially misidentified as electrons, were rejected by cutting on the CC amplitude (> 2 photoelectrons), imposing a minimum energy deposition in the EC (60 MeV) and correlating the measurements of the momentum from the DC and of the energy from the EC. In order to minimize radiative corrections and residual pion contamination, a further cut E$' \geq 0.8$ GeV was also applied, where E$'$ is the scattered electron energy. Finally, vertex and geometric fiducial cuts, which select only regions of well understood acceptance, were included.

The efficiencies of the CC and EC cuts, respectively η_{CC} and η_{EC}, were determined from data samples, selecting unambiguous electrons with very tight CC or EC cuts. The CC-cut efficiencies range from 86 to 99% and the EC-cut efficiencies from 90 to 95%, depending on the electron kinematics. The efficiencies of the geometric fiducial cuts

were derived from CLAS GEANT-based Monte-Carlo simulations.

Pions and protons are identified by the correlation between the momentum measured by the DC and the velocity measured by the SC. This identification procedure is unambiguous for particles with momenta up to 2 GeV. Particles with momenta higher than 2 GeV were therefore discarded. The efficiencies of the cuts imposed for this momentum-velocity correlation and of the geometric fiducial cuts were determined from CLAS GEANT-based Monte-Carlo simulations.

Once the electron, the proton and the positive pion are identified, the $ep \rightarrow e'p\pi^+\pi^-$ final state is identified through the missing mass technique. Fig. 2 shows the square of the missing mass for the system $e'p\pi^+$ (i.e. $M_X^2[e'p\pi^+X]$) as a function of the missing mass for the system ep (i.e. $M_X[e'pX]$). One distinguishes the ρ^0 and ω loci quite clearly. A cut on the $M_X^2[e'p\pi^+X]$ variable is required in order to separate the ρ^0 and the associated $\pi^+\pi^-$ continuum from the ω and the three–pion continuum background. The optimum value of this cut:
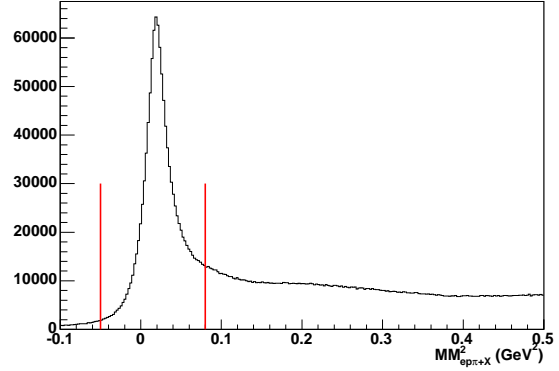
$$-0.05 \leq M_X^2[e'p\pi^+X] \leq 0.08 \text{ GeV}^2 \qquad (1)$$

was determined from a study whereby we estimated the number of ρ^0 events, from fits to the $M_X^2[e'pX]$ distribution, as a function of the cut values. The cuts were chosen in the region where the number of ρ^0 events began to vary only very weakly with these cut values. The simulation used to calculate acceptances reproduces the features of fig. 3. The position of this cut relative to $M_X^2[e'p\pi^+X]$ is shown in fig. 3.
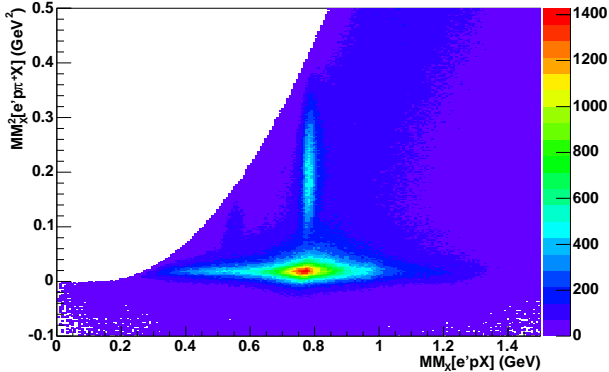

Fig. 2. Squared missing mass $M_X^2[e'p\pi^+X]$ vs $M_X[e'pX]$ for $W \geq 1.8$ GeV and $E' \geq 0.8$ GeV.

The missing mass distribution for the system ep, obtained after this cut, is shown in fig. 4. The ρ^0 peak is very broad : $\Gamma_{\rho^0}^{th} \approx 150$ MeV from ref. [23]. and sits on top of a background of a non-resonant two pion continuum, which originates from other processes leading to the $e'p\pi^+\pi^-$ final state, such as $ep \rightarrow e'\Delta^{++}\pi^- \rightarrow e'p\pi^+\pi^-$. In fig. 4, one can additionnally distinguish two bumps at masses around 950 MeV and 1250 MeV corresponding respectively to the scalar $f_0(980)$ and tensor $f_2(1270)$

Fig. 3. Missing mass $M_X^2[e'p\pi^+X]$ for $W \geq 1.8$ GeV and $E' \geq 0.8$ GeV. The red lines show the cut used (see eq. 1) to select the $e'p\pi^+\pi^-$ final state.

mesons. These will be even more evident when we look at the differential spectra later on.
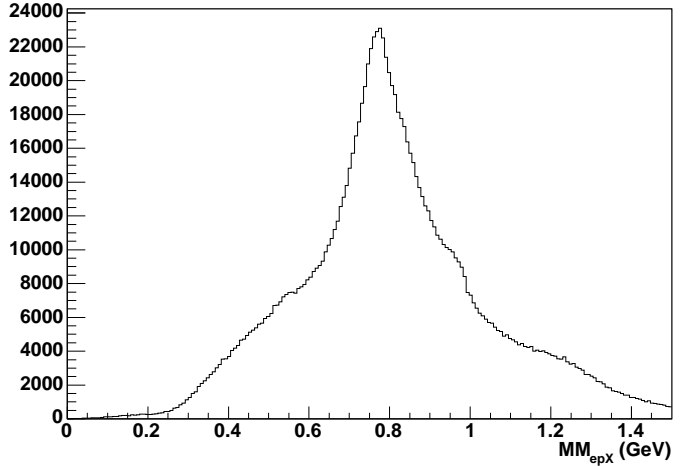
Fig. 4. Missing mass $M_X[e'pX]$ for $-0.05 \leq M_X^2[e'p\pi^+] \leq 0.08$ GeV^2, $W \geq 1.8$ GeV and $E' \geq 0.8$ GeV. The $\rho^0(770)$, as well as the $f_0(980)$ and $f_2(1270)$ resonances which can be distinguished, sits on top of a background of non-resonant two-pion continuum.

2.2 Acceptance calculation

The acceptance of the CLAS detector for the $e'p\pi^+X$ process has been determined with the standard GEANT-based code developed for CLAS. Our event generator [24] contains the three main channels leading to the $e'p\pi^+\pi^-$ final state: $ep \rightarrow e'p\rho^0 \hookrightarrow \pi^+\pi^-$, $ep \rightarrow e'\pi^-\Delta^{++} \hookrightarrow p\pi^+$, and the non-resonant (phase space) $ep \rightarrow e'p\pi^+\pi^-$. This event generator is based on tables of total and differential cross sections of double pion photoproduction data

that have been extrapolated to electroproduction. This has been done by multiplying these tables by a virtual photon flux factor and a dipole form factor in order to obtain a relatively realistic Q^2 dependence of the cross section. We also have tuned the relative weight of all the aforementioned channels in order to reproduce the main kinematical distributions of our experimental data.

Eight independent kinematical variables are necessary to describe a reaction with four particles in the final state. However, in unpolarized electroproduction, the cross section does not depend on the azimuthal angle of the scattered electron. The following seven variables are then chosen: Q^2, x_B, t, $M_{\pi^+\pi^-}$, Φ, $\cos(\theta_{HS})$ and ϕ_{HS}. Here Q^2 and x_B are respectively the absolute value of the squared electron four-momentum transfer and the Bjorken variable, which describe the kinematics of the virtual photon γ^*. At some stages, W, the $\gamma^* - p$ center-of-mass energy will equivalently be used. Then t is the squared four-momentum transferred to the ρ^0, Φ is the azimuthal angle between the electron scattering plane and the hadronic production plane, and $M_{\pi^+\pi^-}$ is the invariant mass of the $\pi^+\pi^-$ system. Finally, $\cos(\theta_{HS})$ and ϕ_{HS} describe the decay of the ρ^0 into two pions and are respectively the polar and azimuthal angles of the π^+ in the so-called Helicity Frame (HS) where the ρ^0 is at rest and the z-axis is given by the ρ^0 direction in the $\gamma^* - p$ center-of-mass system. All these variables are illustrated in fig. 5.
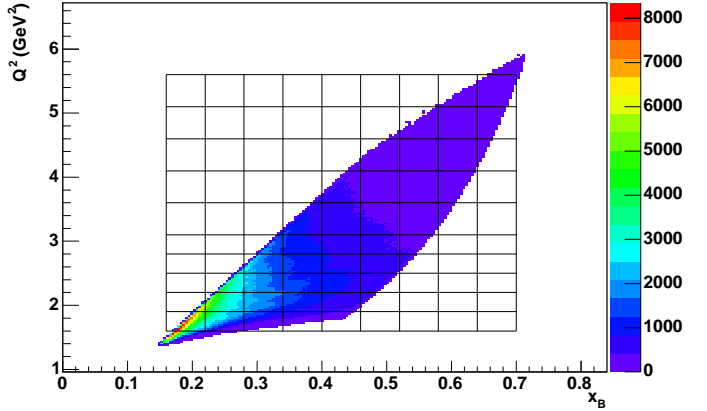
Variable	Unit	Range	# of bins	Width
Q^2	GeV^2	$1.60 - 3.10$	5	0.30
		$3.10 - 5.60$	5	0.50
x_B	–	$0.16 - 0.7$	9	0.06
$-t$	GeV^2	$0.10 - 1.90$	6	0.30
		$1.90 - 4.30$	3	0.80
Φ	deg.	$0.00 - 360.00$	9	40.00
$\cos(\theta_{\pi^+}^{HS})$	–	$-1.00 - 1.00$	8	0.25
$\phi_{\pi^+}^{HS}$	deg.	$0.00 - 360.00$	8	45.00
MM$_{ep}$	GeV	$0.22 - 1.87$	15	0.22

Table 1. Binning in the 7 independent variables for the acceptance table.

Fig. 6. Binning in (Q^2, x_B) for our experimental data (with $W > 1.8$ GeV and $E' \geq 0.8$ GeV).

Fig. 5. Reference frames and relevant variables for the description of the $ep \to e'p\rho^0 \hookrightarrow \pi^+\pi^-$ reaction.

The procedure we have followed has been to calculate an acceptance for each of the 7-dimensional bins. In the limit of small bin-size and unlimited statistics, this procedure is independent of the model used to generate events. Our event generator has nonetheless been tuned to reproduce the experimental data. The binning in the 7 independent variables is defined in table 1 and its 2-dimensional (Q^2, x_B) projection is shown in fig. 6.

More than 200 million Monte-Carlo (MC) events were generated using CLAS GEANT to calculate the accep-

tance in each of the individual 7-dimensional bins. Each "real data" event was then weighted by the ratio of the number of MC generated to accepted events for each 7-dimensional bin. The acceptances are at most a few percent. Bins that have a very small acceptance ($< 0.16\%$) have a very high weight, which produces an unphysically high and narrow peak in the weighted event distributions, and have to be cut away. The efficiency of this cut is evaluated by MC computation of the ratio of weighted accepted events to generated events mapped onto 1-dimensional distributions. This correction factor η_w is therefore model dependent since it is 1-dimensional and thus integrated over the remaining variables. It is on average 15%.

Radiative corrections were part of our event generator and were calculated according to ref. [25]. The MC acceptance calculation presented above therefore took into account the effects of the radiation of hard photons and the corresponding losses due to the application of the cut of eq. 1. The contribution of soft photons and virtual corrections were determined by turning on and off the radiative effects in our event generator, defining an F_{rad} factor for each (Q^2, x_B) bin for the integrated cross sections, or for each (Q^2, x_B, X) bin for the differential cross sections, X being one of t, Φ, $\cos(\theta_{HS})$ or ϕ_{HS}.

2.3 $\gamma^*p \to p\pi^+\pi^-$ **total cross section**

The total reduced cross section for the $ep \to e'p\pi^+\pi^-$ reaction can then be obtained from:

$$\sigma_{\gamma^*p \to p\pi^+\pi^-}(Q^2, x_B, E) = \frac{1}{\Gamma_V(Q^2, x_B, E)} \frac{d^2\sigma_{ep \to e'p\pi^+\pi^-}}{dQ^2 dx_B} \tag{2}$$

with:

$$\frac{d^2\sigma_{ep \to e'p\pi^+\pi^-}}{dQ^2 dx_B} = \frac{n_w(Q^2, x_B)}{\mathcal{L}_{int} \; \Delta Q^2 \; \Delta x_B} \times \frac{F_{rad}}{\eta_{CC}\eta_{EC}\eta_w}, \tag{3}$$

where

- $n_w(Q^2, x_B)$ is the weighted number of $ep \to e'p\pi^+\pi^-$ events in a given bin (Q^2, x_B),
- $\mathcal{L}_{int}$ is the effective integrated luminosity (that takes into account the correction for the data acquisition dead time),
- ΔQ^2 and Δx_B are the corresponding bin widths (see table 1); for bins not completely filled, because of W or E' cuts on the electron for instance (see fig. 6), the phase space $\Delta Q^2 \Delta x_B$ includes a surface correction and the Q^2 and x_B central values are modified accordingly.
- F_{rad} is the correction factor due to the radiative effects (see section 2.2),
- η_{CC} is the CC-cut efficiency (see section 2.1),
- η_{EC} is the EC-cut efficiency (see section 2.1),
- η_w is the efficiency of the cut on the weight in the acceptance calculation (see section 2.2).

We adopted the Hand convention [26] for the definition of the virtual photon flux Γ_V:

$$\Gamma_V(Q^2, x_B, E) = \frac{\alpha}{8\pi} \frac{Q^2}{m_p^2 E^2} \frac{1-x_B}{x_B^3} \frac{1}{1-\epsilon} \tag{4}$$

with

$$\epsilon = \frac{1}{1 + 2\frac{Q^2+(E-E')^2}{4EE'-Q^2}} \tag{5}$$

and $\alpha \approx \frac{1}{137}$ the standard electromagnetic coupling constant.

Fig. 7 shows the total reduced cross section $\sigma_{\gamma^*p \to p\pi^+\pi^-}$ as a function of Q^2 for constant W bins compared with the world's data [18,19,27].

Relatively good agreement between the various experiments can be seen. It is important to realize that what is plotted is the unseparated cross section, i.e. a linear combination of the transverse (σ_T) and longitudinal (σ_L) cross sections : $\sigma = \sigma_T + \epsilon\sigma_L$. This means that, due to ϵ (eq. 5), there is a dependence on the beam energy in this observable. Since the CORNELL data have been taken with an 11.5 GeV electron beam energy [19], the DESY data with a 7.2 GeV electron beam energy [18] and the previous CLAS data with a 4.2 GeV beam [27], the data sets, although at approximatively equivalent Q^2 and W values, are not directly comparable and are not expected to fully match each other. We will come back to this issue in section 2.5 when we are comparing the ρ^0 cross sections.

The next step is to extract the $\gamma^*p \to p\rho^0$ cross section from the $\gamma^*p \to p\pi^+\pi^-$ cross section, which requires a dedicated fitting procedure.

2.4 **Fitting procedure for the** $\gamma^*p \to p\rho^0$ **cross section**

Fig. 8 shows the acceptance-weighted $M_{\pi^+\pi^-}$ spectra for all our (Q^2, x_B) bins. The ρ^0 peak (along with the $f_0(980)$ and $f_2(1270)$ peaks clearly visible in some (Q^2, x_B) bins) sits on top of a $\pi^+\pi^-$ continuum background (see also fig. 4 where all data have been integrated).

This background can be decomposed, in a first approximation, into the non-resonant $ep \to e'p\pi^+\pi^-$ phase space and the exclusive electroproduction of a pion and a nucleon resonance, the latter decaying into a pion and a nucleon, such as $ep \to e'\pi^-\Delta^{++} \hookrightarrow p\pi^+$. Evidence for this can be seen in figs. 9 and 10, which show for all our (Q^2, x_B) bins the acceptance-corrected $p\pi^-$ and $p\pi^+$ invariant-mass spectra where structures are clearly seen. Most of these nucleon resonances (N^*) are rather well known, the most prominent being the $\Delta^{0,++}(1232)$, the $D_{13}(1520)$ and the $F_{15}(1680)$. However, their production amplitudes with an associated pion (i.e. $ep \to e'\pi N^* \hookrightarrow p\pi$) are mostly unknown.

At low energies ($W < 1.8$ GeV) where very few N^* can be produced, a phenomenological model has been developed [28,27] based on an effective Lagrangian where a few N^*'s are superposed along with the production of the ρ^0. Such a model could be a strong constraint and guide to extract the ρ^0 cross section from all the other mechanisms. However, at the present higher energies, numerous new higher mass N^*'s appear as shown by the spectra of figs. 9 and 10. For theoretical calculations, interference effects between all these channels are virtually impossible to control and drastically complicate the analysis. Therefore this approach cannot be pursued in our case.

At present, it is unrealistic to describe simultaneously the $\pi^+\pi^-$, $p\pi^-$ and $p\pi^+$ invariant mass spectra over our entire phase space because there are too many structures varying independently with (Q^2, x_B) in each invariant mass distribution.

Therefore, since a complete description of the di-pion mass spectra is not available, we have adopted an empirical description of the data using non-interfering contributions that, together with a model for the ρ^0 shape, reproduce the $\pi^+\pi^-$ invariant mass spectrum.

The ρ^0 peak is broad and the strength of the non-resonant $\pi^+\pi^-$ background under it is quite significant, and, even more importantly, its nature is unknown. Therefore we must carry out a non-trivial and model-dependent fitting procedure in order to extract the $\gamma^*p \to p\rho^0$ cross section.

The procedure we have followed consisted of fitting only the $M_{\pi^+\pi^-}$ distributions for each (Q^2, x_B) bin in the case of the integrated cross sections and for each (Q^2, x_B, X) bin, where X can be t, Φ, $\cos(\theta_{HS})$ or ϕ_{HS}, in
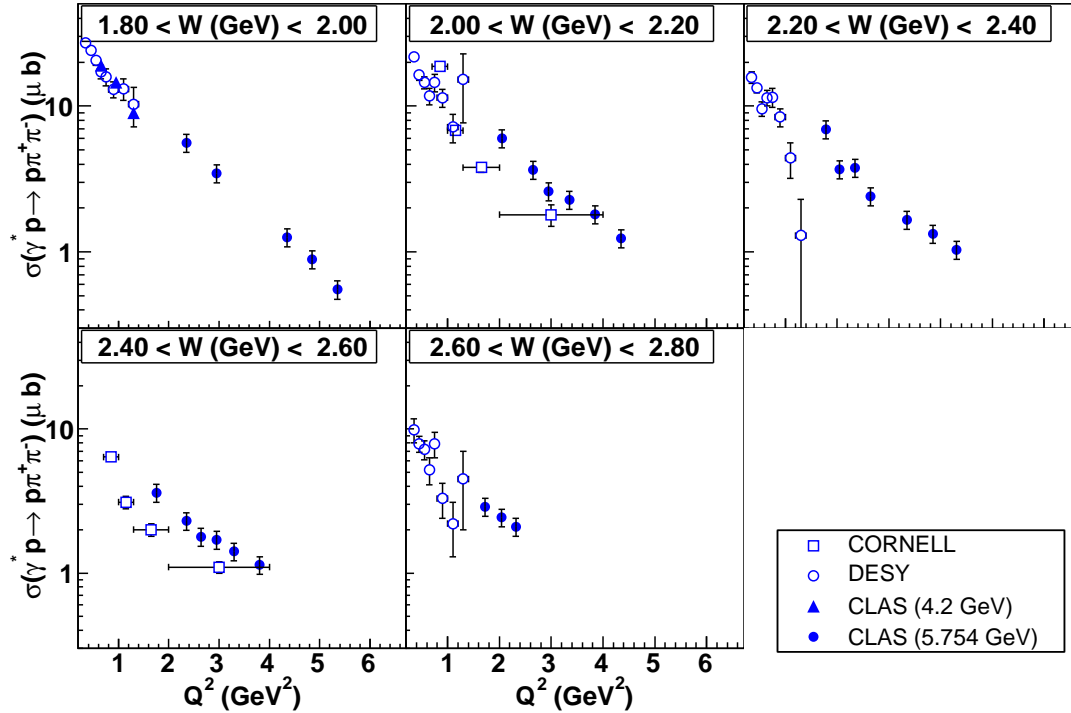
Fig. 7. Reduced cross sections $\gamma^* p \to p\pi^+\pi^-$ as a function of Q^2 for constant W bins, in units of μbarn from the current analysis. Also shown are earlier data from CLAS with a 4.2 GeV beam energy [27] as well as the data from DESY [18] and Cornell [19] with, respectively, a 7.2 GeV and 11.5 GeV beam energy.

the case of the differential cross sections. It was possible to fit the $M_{\pi^+\pi^-}$ spectra with five contributions: three Breit-Wigner shapes to describe the three evident mesonic $\pi^+\pi^-$ resonant structures of the $\rho^0(770)$, $f_0(980)$ and $f_2(1270)$, where the masses in MeV indicated in parentheses are the values given by the Particle Data Group (PDG) [23], and two smoothed histograms that are the $M_{\pi^+\pi^-}$ projections of the reactions $ep \to e'\pi^-\Delta^{++} \hookrightarrow p\pi^+$ and of the non-resonant continuum $ep \to e'p\pi^+\pi^-$. These two latter spectra are calculated by our aforementioned event generator [24]. We now detail these five contributions and explain why they are necessary (and sufficient).

We first discuss the contribution of the $\rho^0(770)$ and the way to model it. It is well known that simple symmetric Breit-Wigner line shapes which are, to first order, used to describe resonances, are too naive to reproduce the ρ shape, because of, among other aspects, interference effects with the non-resonant $\pi^+\pi^-$ continuum. Several methods can be found in the literature for treating the ρ^0 shape (see for instance ref. [29] for such a discussion). The procedure we adopted was the following:

– Introduction of an energy-dependent width in order to take into account that the ρ^0 is an unstable spin-1 particle that decays into two spin-0 particles; it is also called a p-wave Breit-Wigner [30]. This modified

Breit-Wigner reads:

$$BW_\rho(M_{\pi^+\pi^-}) = \frac{M_\rho \Gamma(M_{\pi^+\pi^-})}{(M_\rho^2 - M_{\pi^+\pi^-}^2)^2 + M_\rho^2 \Gamma_\rho^2(M_{\pi^+\pi^-})} \quad (6)$$

with the energy-dependent width:

$$\Gamma^\rho(M_{\pi^+\pi^-}) = \Gamma_\rho \left(\frac{q}{q_\rho}\right)^{2l+1} \frac{M_\rho}{M_{\pi^+\pi^-}}, \quad (7)$$

where $l = 1$ for a p-wave Breit-Wigner, q is the momentum of the decay pion in the ρ^0 center-of-mass frame and q_ρ is equal to q for $M_{\pi^+\pi^-} = M_\rho$:

$$q = \frac{\sqrt{M_{\pi^+\pi^-}^2 - 4M_\pi^2}}{2}, \quad q_\rho = \frac{\sqrt{M_\rho^2 - 4M_\pi^2}}{2}. \quad (8)$$

– Ross and Stodolsky [31] and Söding [32] have shown that the interferences between the broad ρ^0 peak and the important non-resonant $\pi^+\pi^-$ contribution underneath leads to a skewing of the Breit-Wigner. According to Ross-Stodolsky, one way to take account of this effect is to introduce a correction term that consists of multiplying the Breit-Wigner formula by an empirical factor that shifts the centroid of the $M_{\pi^+\pi^-}$ distribution:

$$BW_\rho^{sk\cdot}(M_{\pi^+\pi^-}) = BW_\rho(M_{\pi^+\pi^-}) \left(\frac{M_\rho}{M_{\pi^+\pi^-}}\right)^{n_{skew}} \quad (9)$$
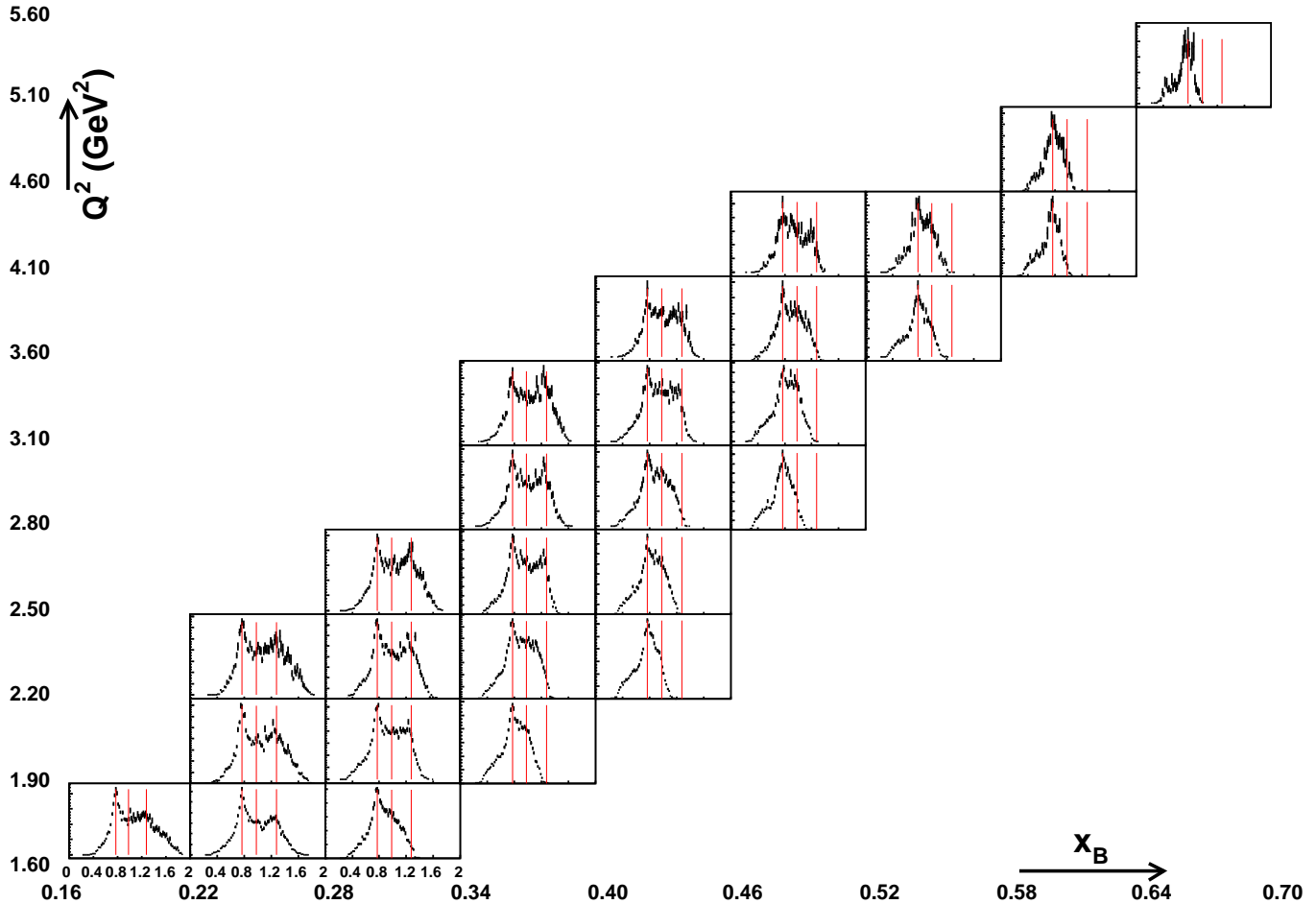
Fig. 8. Acceptance-corrected $M_X[e'pX]$ (in GeV) missing mass spectra for all our (Q^2, x_B) bins. The three red lines are located at $M_X = 0.770, 0.980, 1.275$ GeV corresponding to the three well-known resonant states in the $(\pi^+\pi^-)$ system.

where n_{skew} is the "skewing" parameter. Although Ross-Stodolsky have predicted the value of n_{skew} to be 4, it is often a parameter that is fitted to the data since so little is known concerning the interference between the ρ^0 signal and the $\pi^+\pi^-$ continuum.

As is evident in fig. 8, in addition to the $\rho^0(770)$, there are two well-known resonant structures in the $\pi^+\pi^-$ system: the $f_0(980)$ and $f_2(1270)$. Due to the large widths of these mesonic resonances (40 to 100 MeV [23] for the $f_0(980)$ and ≈ 180 MeV [23] for the $f_2(1270)$), it is clearly necessary to include them in our $M_{\pi^+\pi^-}$ fit because their contribution can extend into the ρ^0 region, which is itself also broad. We also used the formulas of eqs. 6-9 for these two other mesonic resonant states $f_0(980)$ and $f_2(1270)$ with appropriate parameters M_{f_0}, Γ_{f_0}, M_{f_2}, Γ_{f_2} and took into account their $l = 0$ and $l = 2$ nature.

In principle, the only free parameter to vary in eq. 9 should be n_{skew}. However, we have also allowed the central masses and widths of the three mesons to vary in a very limited range of at most 20 MeV from their nominal values (see table 2). The motivation for this is that, besides the largely unknown interference effects between the meson and the $\pi^+\pi^-$ continuum, several other effects can

shift or distort the meson shapes: radiative corrections, binning, acceptance corrections, imprecise values for the central masses and widths of some of these mesons, etc.

Finally, besides the ρ^0, $f_0(980)$ and $f_2(1270)$ mesons, the two other contributions entering our fit are: the $M_{\pi^+\pi^-}$ projections of the reactions $ep \to e'\pi^-\Delta^{++} \hookrightarrow p\pi^+$ and the non-resonant continuum (phase space) $ep \to e'p\pi^+\pi^-$. The shapes of these distributions are given by our event generator. In particular, the Δ^{++} has the shape of a standard Breit-Wigner in the $p\pi^+$ distribution with a centroid at 1.232 GeV and a width of 111 MeV [23]. As is obvious from fig. 9, the Δ^0 contribution can be neglected.

In principle, of course, other processes contribute to the $M_{\pi^+\pi^-}$ continuum, for instance all of the $ep \to e\pi^- N^* \hookrightarrow p\pi^+$ reactions, as already mentioned. As a test, we modeled the $p\pi^-$ and $p\pi^+$ invariant mass distributions of figs. 9 and 10 by adding, at the cross section level, several Breit-Wigners matching the structures seen in these figures and identifying them with known N^* masses (and widths) that can be found in the PDG. Like for the Δ^{++}, we introduced their contribution into our fit of the $M_{\pi^+\pi^-}$ distribution using our event generator. The conclusion we reached was twofold. Firstly, this procedure introduced a large number of additional free parameters: for each of the extra N^*'s,
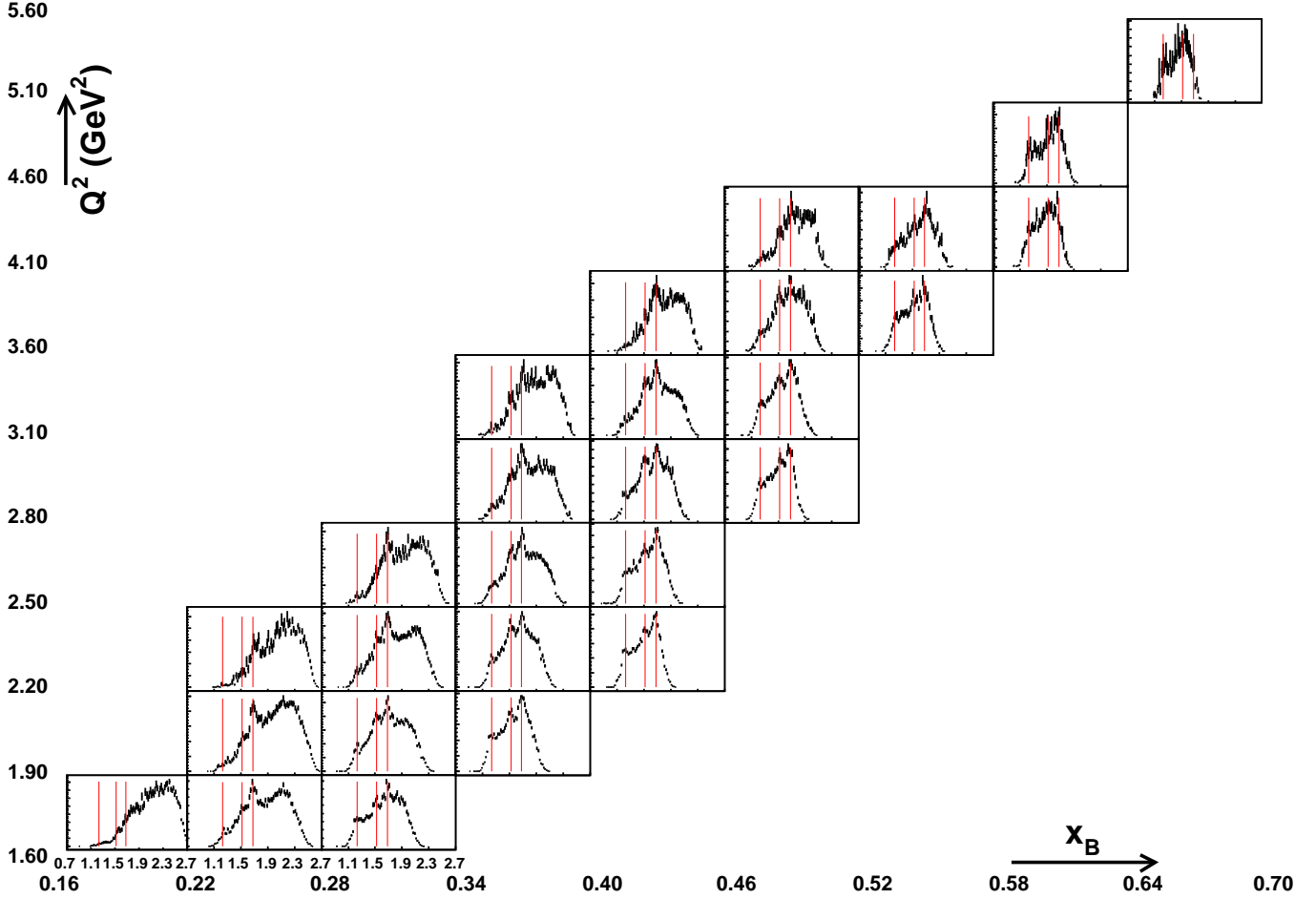
Fig. 9. Acceptance-corrected $M_{p\pi^-}$ (in GeV) invariant mass distributions for all our (Q^2, x_B) bins. The three red lines are located at $M_X = 1.232, 1.520, 1.680$ GeV corresponding to three well-known resonance regions in the $(p\pi^-)$ system.

parameter	PDG value	min. value	max. value
ρ^0 mass M_ρ (MeV)	≈ 770	750	790
ρ^0 width Γ_ρ (MeV)	≈ 150	140	170
f_0 mass M_{f_0} (MeV)	≈ 980	970	990
f_0 width Γ_{f_0} (MeV)	40-100	40	120
f_2 mass M_{f_2} (MeV)	≈ 1275	1260	1280
f_2 width Γ_{f_2} (MeV)	≈ 185	170	200

**Table 2.** Range of variations permitted for the parameters to be fitted in formula 9.

two parameters for the central mass and width to vary in the approximate ranges given by the PDG and one more for the weight/normalization. Secondly, we found that the $M_{\pi^+\pi^-}$ projected shape of these high mass N^*'s was very similar to the phase-space $M_{\pi^+\pi^-}$ distribution. In other words, in a first approximation, the phase-space contribution can reflect and absorb the high mass N^*'s. However, the Δ^{++} contribution to the $M_{\pi^+\pi^-}$ distribution was found to be sufficiently different from the phase space distribution to be kept as an individual contribution.

To summarize, each (Q^2, x_B) bin of fig. 8 was fit with the following formula:

$$\frac{dN}{dM_{\pi^+\pi^-}} = BW_\rho(M_{\pi^+\pi^-})$$
$$+ BW_{f_0}(M_{\pi^+\pi^-}) + BW_{f_2}(M_{\pi^+\pi^-})$$
$$+ M_{\Delta^{++}\pi^-}(M_{\pi^+\pi^-}) + M_{p\pi^+\pi^-}(M_{\pi^+\pi^-})$$

(10)

It involves 14 parameters that are:

- 1) weight (normalization), 2) central mass, 3) width and 4) n_{skew} of ρ^0;
- 5) weight (normalization), 6) central mass, 7) width and 8) n_{skew} of f_0;
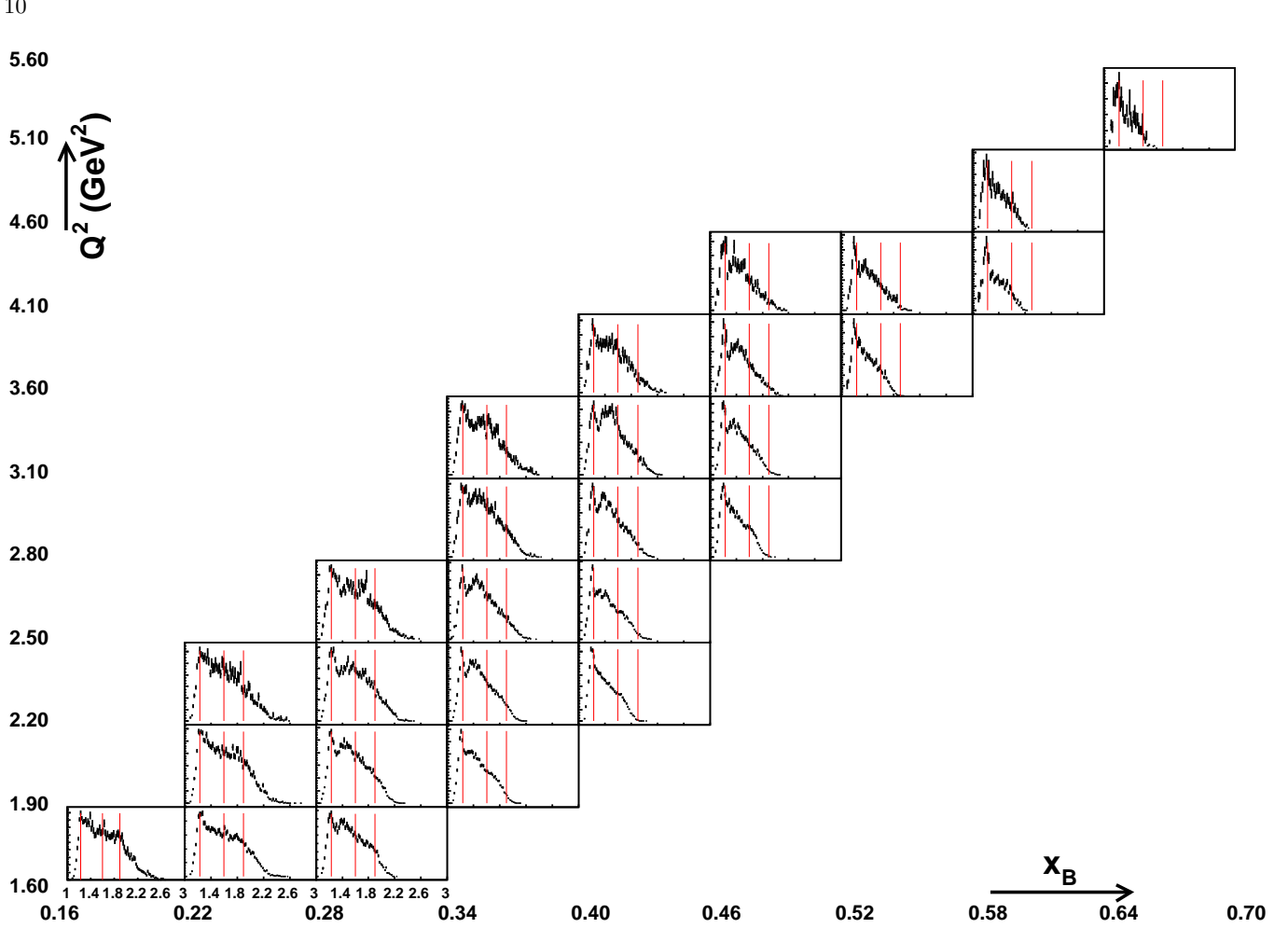
Fig. 10. Acceptance-corrected $M_{p\pi^+}$ (in GeV) invariant mass distributions for all our (Q^2, x_B) bins. The three red lines are located at $M_X = 1.232, 1.600, 1.900$ GeV corresponding to the three well-known resonance regions in the ($p\pi^+$) system.

- 9) weight (normalization), 10) central mass, 11) width and 12) n_{skew} of f_2;
- 13) weight (normalization) of $M_{\pi^+\pi^-}$ projection of the $ep \rightarrow e'\pi^-\Delta^{++} \hookrightarrow p\pi^+$ process; and
- 14) weight (normalization) of $ep \rightarrow e'p\pi^+\pi^-$ phase space.

Fourteen parameters might appear a lot to fit only a 1-dimensional distribution. However, on the one hand, six of these (the central mass and width of the ρ^0, $f_0(980)$ and $f_2(1270)$ mesons) are quite constrained and are allowed to vary in a very limited range. On the other hand this simply reflects the complexity and our lack of knowledge of the $ep \rightarrow e'p\pi^+\pi^-$ reaction, to which many unknown, independent though interfering processes contribute; namely: meson production $ep \rightarrow e'pM^0 \hookrightarrow \pi^+\pi^-$, N^* production $ep \rightarrow e'\pi^-N^{*++} \hookrightarrow p\pi^+$, $ep \rightarrow e'\pi^+N^{*0} \hookrightarrow p\pi^-$, non-resonant $ep \rightarrow e'p\pi^+\pi^-$, etc.

Fig. 11 shows the result of our fits to the $M_{\pi^+\pi^-}$ distributions, normalized in terms of the reduced cross sections of eq. 3 for all of our (Q^2, x_B) bins. In a few cases, the fits do not fully describe the data. For instance, for $0.46 < x_B < 0.52$, $3.10 < x_B < 3.60$, the data tend to show a "structure" around $M_{\pi^+\pi^-}$=0.9 GeV, i.e. between the

known ρ^0 and f_0 resonances, which cannot be reproduced by our fit formula of eq. 10. We attribute this discrepancy to interference effects not taken into account by our simple fit procedure. As discussed in more detail in the next subsections, a systematic uncertainty of 25% is assigned to this whole fit procedure which is meant to account, among other aspects, for the inadequacies in the model. On all the figures that are going to be presented from now on, unless explicitly stated otherwise, all the error bars associated to our data points will represent the quadratic sum of the statistical and systematic errors.

2.5 Integrated ρ^0 cross section

We use the ρ^0 strength (green line) extracted from the distributions shown in fig. 11 to calculate the cross section. Fig. 12 shows the resulting reduced cross section $\sigma_{\gamma^*p \rightarrow p\rho^0}$ compared with the world's data presented as a function of W for constant Q^2 bins. Fig. 13 shows the reduced cross section $\sigma_{\gamma^*p \rightarrow p\rho^0}$ compared with the world's data presented as a function of Q^2 for constant W bins.

With respect to the $\gamma^*p \rightarrow p\pi^+\pi^-$ cross section that we extracted in the previous section, there is an additional
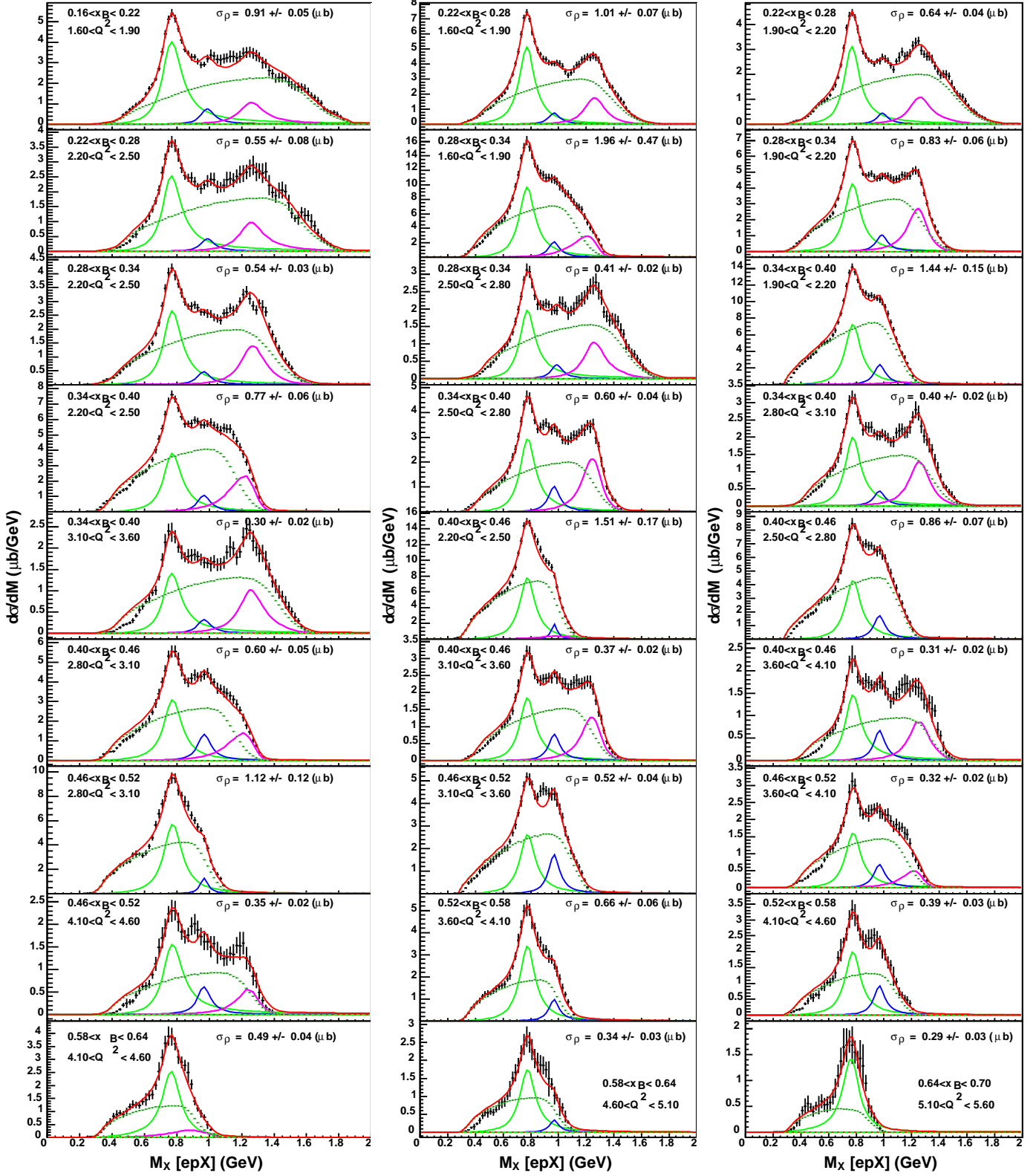
Fig. 11. Acceptance-corrected $M_X[e'pX]$ missing mass distributions , showing our fits. In red: total fit result; in green: ρ^0 contribution; in blue: f_0 contribution; in purple: f_2 contribution and in dotted green: $\pi^+\pi^-$ continuum, which is the sum of the $ep \rightarrow e'\pi^-\Delta^{++} \hookrightarrow p\pi^+$ projections on $M_{\pi^+\pi^-}$ and of the phase space $ep \rightarrow e'p\pi^+\pi^-$ contributions. The error bars on the data points are purely statistical. The uncertainties on the cross sections given by the fit is also purely statistical.
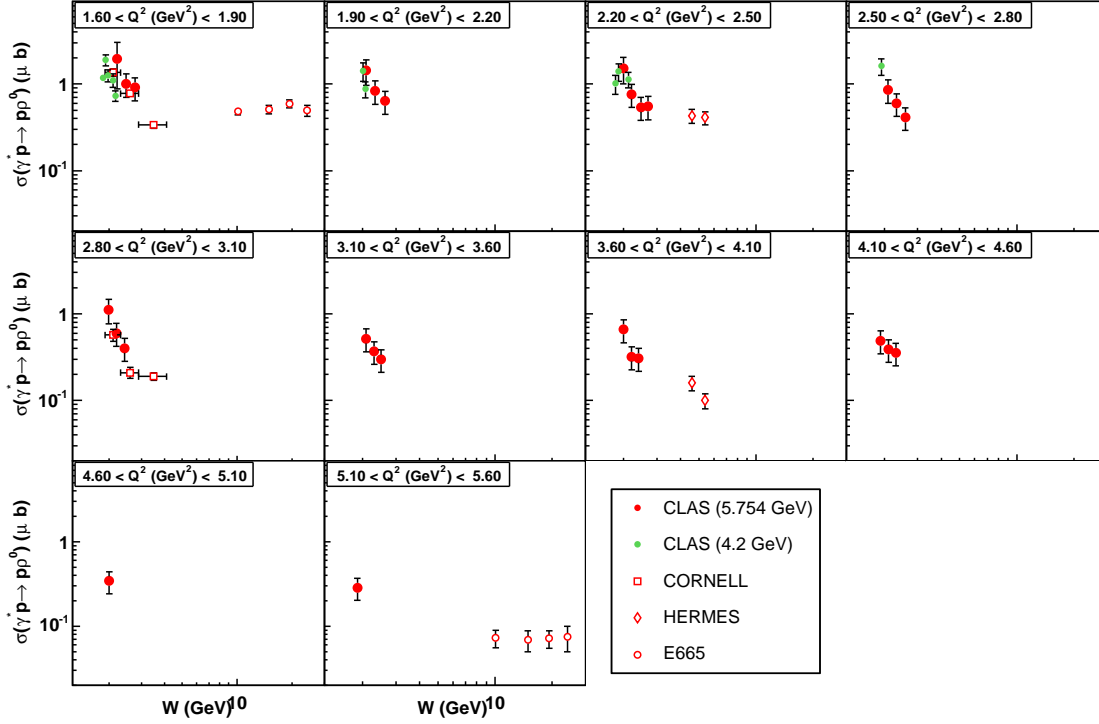
Fig. 12. Reduced cross sections $\gamma^* p \to p\rho^0$ as a function of W for constant Q^2 bins, in units of μbarn. The error bars of the CLAS data result from the quadratic sum of the statistical and systematic uncertainties. The horizontal error bars of the Cornell data indicate their W range. The 4.2 GeV CLAS, CORNELL, HERMES and E665 data are respectively from refs. [21], [19], [20] and [33].

source of systematic uncertainty for the $\sigma_{\gamma^* p \to p\rho^0}$ cross section that arises from the subtraction procedure described in the previous section. This contribution is quite difficult to evaluate. It is not so much the quality of the fit in fig. 11 that matters; we have varied the minimum and maximum limits imposed on the parameters in table 2 and found that the results of the fits are very stable. The uncertainty arises more from the reliability and confidence we can assign to the modeling that we have adopted for the ρ^0, $f_0(980)$ and $f_2(1270)$ mesons with the skewed Breit-Wigners and for the non-resonant continuum $\pi^+\pi^-$ distribution. We have tried several shapes for this latter continuum. As mentioned in the previous subsection, we introduced N^* states other than the Δ^{++}. Ultimately, we ended up finding the fits to be stable at the ≈ 20 % level on average. Overall, we cannot take account of any interference effects between the ρ^0 peak and the non-resonant $\pi^+\pi^-$ continuum. This uncertainty is of a theoretical nature, and in the absence of sufficient guidance at present, we have decided to assign a relatively conservative 25% systematic uncertainty to our extracted ρ^0 yields. We will find some relative justification for this estimation in the next section when we study the differential distributions, in particular those of t and $\cos\theta_{HS}$.

Recently, a partial wave analysis of data of exclusive $\pi^+\pi^-$ photoproduction on the proton from CLAS, has been carried out [34]. This study showed that the ρ^0 cross

sections resulting from this sophisticated method were consistent with those resulting from simple fits of the two-pion invariant mass as we have just described, to a level much lower than 25%. Although no such partial wave analysis has been done to the present electroproduction data, this photoproduction comparison gives relative confidence that the 25% systematic uncertainty that we presently assign, is rather conservative.

Coming back to fig. 12, we find that our data are in general agreement with the other world's data in regions of overlap. In the upper left plot of fig. 12 (1.60< Q^2 <1.90 GeV^2), our CLAS (5.754 GeV) data seem to overestimate the CLAS (4.2 GeV) results, but this can certainly be attributed to a kinematic effect due to the different beam energies of the two data sets. Indeed, we are comparing the total reduced cross sections : $\sigma = \sigma_T + \epsilon\sigma_L$. However, at W=2.1 GeV and Q^2=1.7 GeV^2, ϵ=0.53 for a 4.2 GeV beam energy but ϵ=0.77 for a 5.754 GeV beam energy. This can readily explain the lower CLAS (4.2 GeV) data with respect to the CLAS (5.754 GeV) data.

On this general account, we could have expected that the Cornell data stand to some extent above the CLAS (5.754 GeV) data since they have been obtained with an 11.5 GeV beam energy. This is not the case which might indicate a slight incompatibility between the Cornell and CLAS data. This point, as well as the compatibility of the CLAS (4.2 GeV) and CLAS (5.754 GeV) data, will be
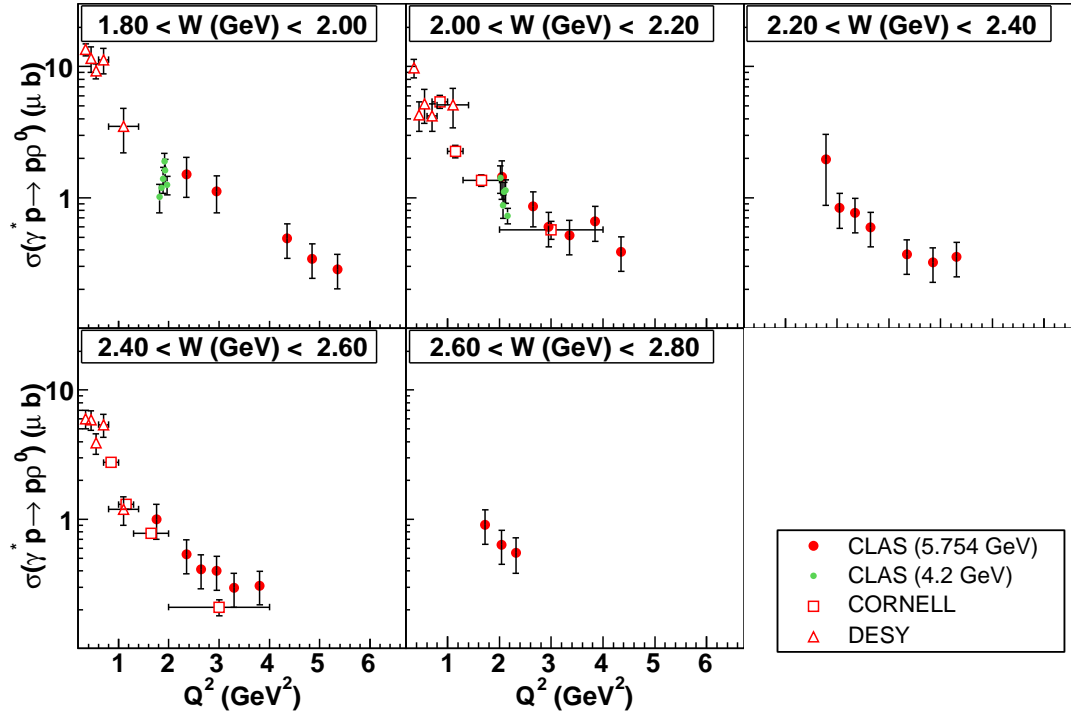
Fig. 13. Reduced cross sections $\gamma^*p \rightarrow p\rho^0$ as a function of Q^2 for constant W bins, in units of μbarn. The 4.2 GeV CLAS, CORNELL and DESY data are respectively from refs. [21], [19] and [18].

confirmed in section 3.3 where we compare the separated longitudinal and transverse cross sections for which this beam energy kinematical effect is removed.

2.6 Differential ρ^0 cross sections

After having obtained the total ρ^0 cross section, we now extract the differential cross sections in t, Φ, $\cos(\theta_{HS})$ and ϕ_{HS}.

Since the data are now binned in an additional variable, each bin has fewer statistics, not only for the real data but also for the MC data that are necessary to calculate the acceptance correction. Bins for which η_w is less than 0.6 were rejected, where, we recall, η_w is the correction factor in the acceptance calculation that was introduced in section 2.2. This explains why some holes occur at several instances, in particular in the Φ and $\cos(\theta_{HS})$ distributions.

We start by extracting the $d\sigma/dt$ cross section. Defining t' as $t - t_0$, where t_0 is the maximum t value kinematically allowed for a given (Q^2, x_B) bin, we divided the data into 6 bins for $0 < -t' < 1.5$ GeV^2 and 3 bins for $1.5 < -t' < 3.9$ GeV^2. For each of the (t, Q^2, x_B) bins, we extracted the ρ^0 signal from the (π^+, π^-) invariant mass spectra using the fitting procedure previously described.

Fig. 14 shows $d\sigma/dt$ for all our (Q^2, x_B) bins as a function of t. The general feature of these distributions is that they are of a diffractive type, i.e. proportional to e^{bt}. The

values of the slope b are between 0 and 3 GeV^{-2}. They are plotted as a function of W in fig. 15 along with the world's data. For the sake of clarity, only the world's data for $Q^2 > 1.5$ GeV^2 are displayed. For $Q^2 < 1.5$ GeV^2, the data show the same trend but with more dispersion. The data exhibit a rise with W until they reach a plateau around $W = 6$ GeV at a b value of ≈ 7 GeV^{-2}. The high-energy experiments (H1 and ZEUS) have shown that this saturating value tends to decrease with Q^2, which is illustrated by the H1 points in fig. 15 that correspond to different Q^2 values.

By integrating the $d\sigma/dt$ cross section, we are able to recover at the $\approx 20\%$ level the integrated cross sections that were presented in section 2.5. The agreement is not perfect since for the integrated cross section one fits a single full statistics $M_{\pi^+\pi^-}$ spectrum, whereas for the differential cross section, one fits several lower statistics $M_{\pi^+\pi^-}$ spectra, that are then summed. This relatively good agreement serves, among other arguments, to justify the 25% systematic uncertainties that we have applied in the non-resonant $\pi^+\pi^-$ background subtraction procedure.

We note that the integrated cross sections that we have presented so far (and which will be presented in the remainder of this article) have been summed over only the domain where we had data and acceptance. We have not extrapolated our cross sections beyond the t domain accessed in this experiment, which we deem unsafe and very model-dependent. Fig. 14 indicates that this might underestimate some integrated cross sections for a (very limited)
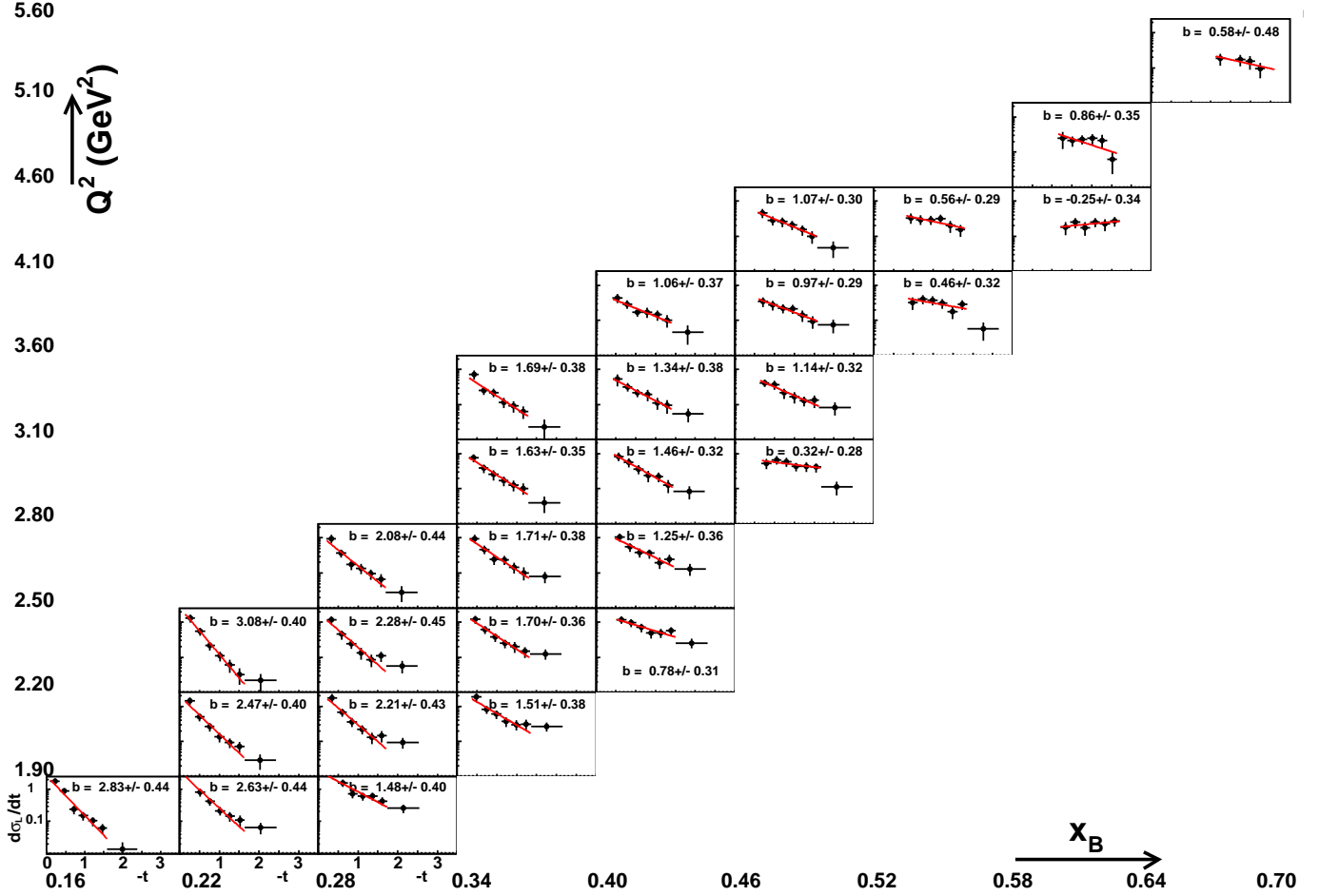
Fig. 14. Cross section $d\sigma/dt$ (in μb/GeV^2) for all bins in (Q^2, x_B) as a function of $-t$ (in GeV^2). The red line shows the fit to the function e^{bt} over the limited range $0 < -t' < 1.5$ GeV^2.

number of (Q^2, x_B) bins at large x_B, where the t dependence appears rather flat.

We proceeded in the same way to extract $d\sigma/d\Phi$. All of our (Q^2, x_B) bins are shown in fig. 16. Several of the bins near $\Phi = 180^o$ are empty or have large error bars because of very low acceptance in CLAS in this region.

These distributions were fitted with the expected Φ dependence for single meson electroproduction:

$$\frac{d\sigma}{d\Phi} = \frac{1}{2\pi}(\ \sigma_T + \epsilon\sigma_L$$
$$+ \epsilon\cos 2\Phi \ \sigma_{TT} + \sqrt{2\epsilon(1+\epsilon)}\cos\Phi \ \sigma_{TL}) \tag{11}$$

from which we could extract the interference terms σ_{TT} and σ_{TL}. The curves in fig. 16 show the corresponding fits, and $\sigma_T + \epsilon\sigma_L$, σ_{TT} and σ_{TL} are displayed in fig. 17. If helicity is conserved in the s channel (SCHC), the interference terms σ_{TT} and σ_{TL} would vanish. Most of our extracted values are consistent with 0 within (large) error bars, although one clearly cannot make strong claims about SCHC at this point.

Turning to the pion decay angles of the ρ^0, θ_{HS} and ϕ_{HS}, they are expected to follow the general and model independent distribution [40]:

$$W(\Phi, \cos\theta_{HS}, \varphi_{HS}) =$$
$$\frac{3}{4\pi}\left[\frac{1}{2}(1 - r_{00}^{04}) + \frac{1}{2}(3r_{00}^{04} - 1)\cos^2\theta_{HS}\right]$$
$$-\sqrt{2}\mathrm{Re}r_{10}^{04}\sin 2\theta_{HS}\cos\varphi_{HS} - r_{1-1}^{04}\sin^2\theta_{HS}\cos 2\varphi_{HS}$$
$$-\epsilon\cos 2\Phi(r_{11}^1\sin^2\theta_{HS} + r_{00}^1\cos^2\theta_{HS}$$
$$-\sqrt{2}\mathrm{Re}r_{10}^1\sin 2\theta_{HS}\cos\varphi_{HS} - r_{1-1}^1\sin^2\theta_{HS}\cos 2\varphi_{HS})$$
$$-\epsilon\sin 2\Phi(\sqrt{2}\mathrm{Im}r_{10}^2\sin 2\theta_{HS}\sin\varphi_{HS}$$
$$+\mathrm{Im}r_{1-1}^2\sin^2\theta_{HS}\sin 2\varphi_{HS})$$
$$+\sqrt{2\epsilon(1+\epsilon)}\cos\Phi(r_{11}^5\sin^2\theta_{HS} + r_{00}^5\cos^2\theta_{HS}$$
$$-\sqrt{2}\mathrm{Re}r_{10}^5\sin 2\theta_{HS}\cos\varphi_{HS} - r_{1-1}^5\sin^2\theta_{HS}\cos 2\varphi_{HS})$$
$$+\sqrt{2\epsilon(1+\epsilon)}\sin\Phi(\sqrt{2}\mathrm{Im}r_{10}^6\sin 2\theta_{HS}\sin\varphi_{HS}$$
$$+\mathrm{Im}r_{1-1}^6\sin^2\theta_{HS}\sin 2\varphi_{HS}) \ ], \tag{12}$$

where:

$$r_{ij}^{04} = \frac{\rho_{ij}^0 + \epsilon R\rho_{ij}^4}{1 + \epsilon R}$$

$$r_{ij}^\alpha = \frac{\rho_{ij}^\alpha}{1 + \epsilon R} \quad \alpha = 1, 2$$
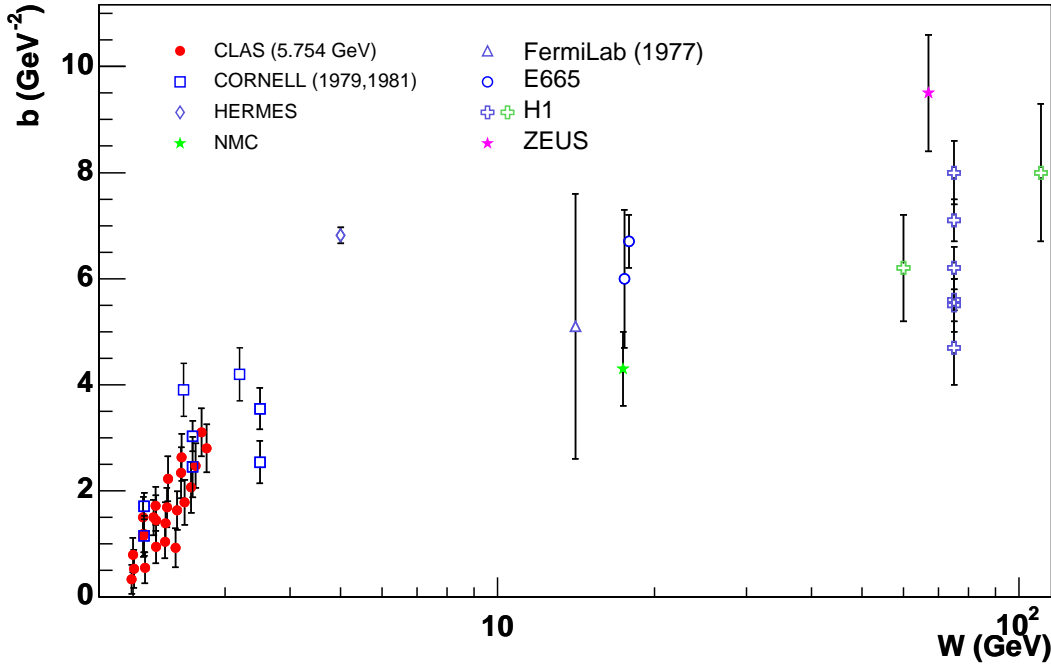
Fig. 15. Slope b of $d\sigma/dt$ as a function of W. Data of Cornell [19,35], HERMES [20], NMC [36], Fermilab (1979) [37], E665 [33], H1 [38] and ZEUS [39] are shown for comparison.

$$r_{ij}^{\alpha} = \sqrt{R}\,\frac{\rho_{ij}^{\alpha}}{1+\epsilon R} \quad \alpha = 5,6 \qquad (13)$$

with R_{ρ} equal to the ratio σ_L/σ_T.

The parameters ρ_{ij}^{α} are bilinear combinations of the helicity amplitudes that describe the $\gamma^* p \to \rho^0 p$ transition. They come from a decomposition of the 3×3 spin density matrix of the ρ^0 in a basis of 9 hermitian matrices. The superscript α refers to the virtual photon polarization: $\alpha = 0$-2 for transverse photons, $\alpha = 4$ for longitudinal photons, and $\alpha = 5$-6 for the interference between L and T terms. The subscript refers to the vector meson helicity: $i, j = 0$ refers to a longitudinal polarization state and $i, j = -1, 1$ to a transverse polarization state. For example, ρ_{00}^0 is related to the probability of the transition between a transverse photon ($\alpha = 0$) and a longitudinal meson ($i, j = 0$) and ρ_{01}^0 is an interference term between meson helicities 0 and 1 ($i = 0, j = 1$) produced by a transverse photon ($\alpha = 0$).

If SCHC applies, then by definition, $\rho_{00}^0 = 0$ and $\rho_{00}^4 = 1$. Then eq. 13 leads to a direct relation between the measured r_{00}^{04} and the ratio $R_{\rho} = \frac{\sigma_L}{\sigma_T}$. In that case, the longitudinal and transverse cross sections, σ_L and σ_T, may be extracted from the $\cos\theta_{HS}$ distribution, without relying on a delicate Rosenbluth separation.

SCHC can be tested by studying the integrated distributions $W(\phi_{HS})$ and $W(\Psi)$ (where $\Psi = \phi_{HS} - \Phi$) over the other decay angles. Integrating $W(\Phi, \cos\theta_{HS}, \phi_{HS})$ of

eq. 12 over $\cos\theta_{HS}$ and Φ yields:

$$W(\phi_{HS}) = \frac{1}{2\pi}\left[1 - 2r_{1-1}^{04}\cos 2\phi_{HS}\right], \qquad (14)$$

which isolates r_{1-1}^{04}, a density matrix element violating SCHC. Integrating $W(\Phi, \cos\theta_{HS}, \phi_{HS})$ over $\cos\theta_{HS}$ yields:

$$W(\Psi) = \frac{1}{2\pi}\left[1 + 2\epsilon r_{1-1}^1\cos 2\Psi\right]. \qquad (15)$$

Another consequence of SCHC is that the $W(\phi_{HS})$ distribution should be constant and the $W(\Psi)$ distribution should vary as $\cos 2\Psi$ if r_{1-1}^1 is not zero.

We extracted the $d\sigma/d\phi_{HS}$ and $d\sigma/d\Psi$ cross sections in the same way as previously mentioned, i.e. by fitting the $M_X[e'pX]$ spectra and extracting the ρ^0 yield for each (Q^2, x_B, ϕ_{HS}) and (Q^2, x_B, Ψ) bin, respectively. Fig. 18 shows the extracted values of r_{1-1}^{04} and r_{1-1}^1, obtained by fitting $d\sigma/d\phi_{HS}$ and $d\sigma/d\Psi$ with the functions of eqs. 14 and 15, respectively. Basically all the SCHC violating matrix elements r_{1-1}^{04} are compatible with 0 (though within large uncertainties), which gives some relative confidence in the validity of SCHC. In addition, r_{1-1}^1 is also found to be compatible with 0 for all kinematics, although this is not a necessary requirement for SCHC. This indicates that our Ψ distributions are basically flat.

We finally extract the r_{00}^{04} matrix element from the $\cos\theta_{HS}$ distributions, which result from the integration of
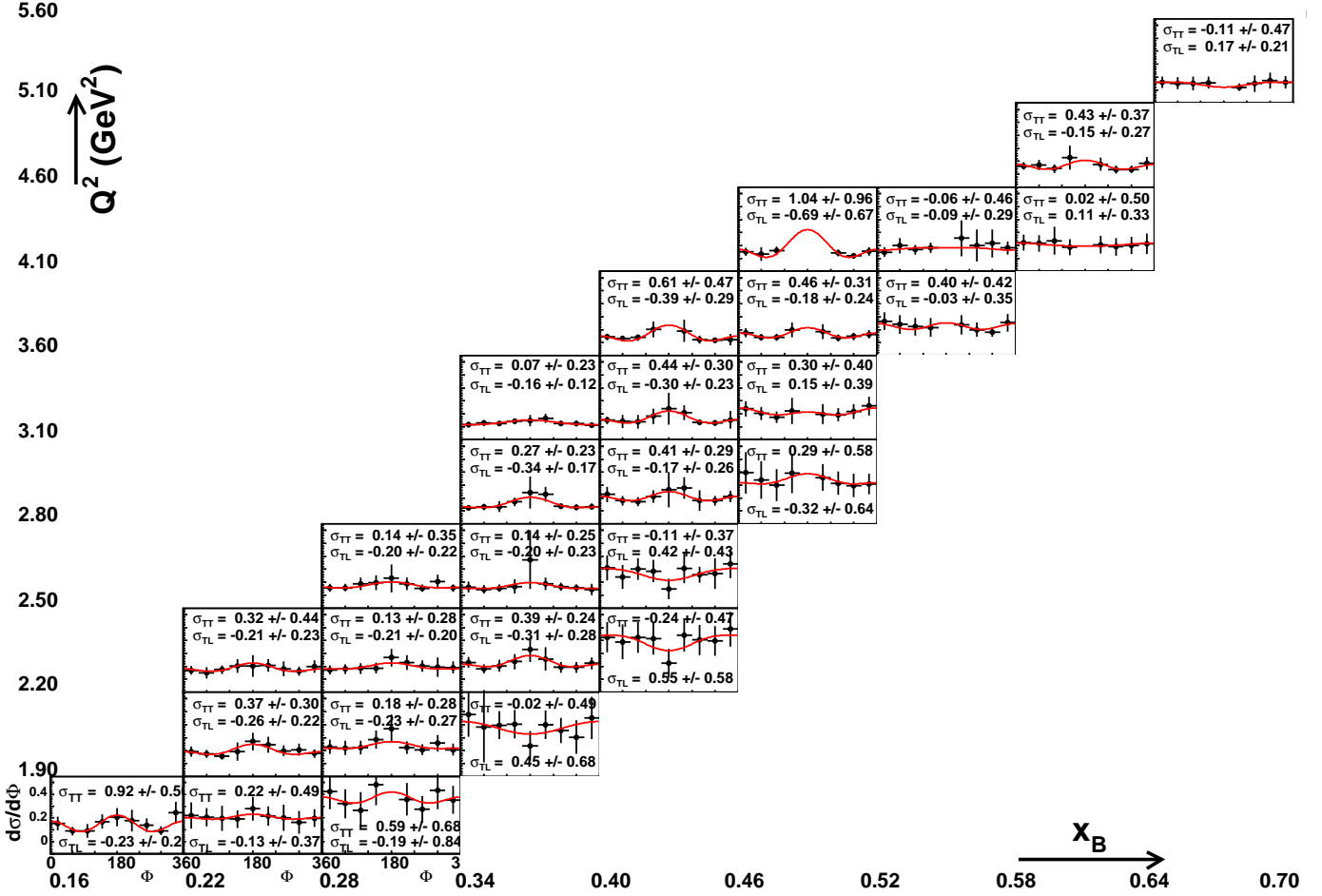
Fig. 16. Cross section $d\sigma/d\Phi$ (in μb/rad) for all bins in (Q^2, x_B) as a function of Φ (in deg.).

$W(\Phi, \cos\theta_{HS}, \phi_{HS})$ of eq. 12 over ϕ_{HS} and Φ:

$$W(\cos\theta_{HS}) = \frac{3}{8}\left[(1 - r_{00}^{04}) + (3r_{00}^{04} - 1)\cos^2\theta_{HS}\right]. \quad (16)$$

As an example, fig. 19 shows a $\cos\theta_{HS}$ distribution, before and after the non-resonant $\pi^+\pi^-$ background subtraction, for one of our typical (Q^2, x_B) bins. We note that the unsubtracted distribution is highly asymmetrical in $\cos\theta_{HS}$. This is mainly due to the presence of events from the $ep \to e'\Delta^{++}\pi^-$ reaction, whose phase space is maximum around $\cos\theta_{HS} = 1$.

Fig. 20 shows the $d\sigma/d\cos(\theta_{HS})$ cross sections for all bins in (Q^2, x_B). Even after the non-resonant $\pi^+\pi^-$ background subtraction procedure, some of the aforementioned asymmetry in the $\cos(\theta_{HS})$ distribution remains at the $\approx 25\%$ level. We attribute this to interference effects between the ρ^0 channel and its background (mostly, $ep \to e'\pi^-\Delta^{*++} \hookrightarrow p\pi^+$ and non-resonant $ep \to e'p\pi^+\pi^-$ as already discussed), which obviously cannot be taken into account when subtracting the different channels at the cross-section level as we do. This $\approx 25\%$ $\cos\theta_{HS}$ asymmetry is a further confirmation of the systematic uncertainty associated to the extraction of the ρ^0 signal. Fig. 18 shows then the resulting r_{00}^{04} values.
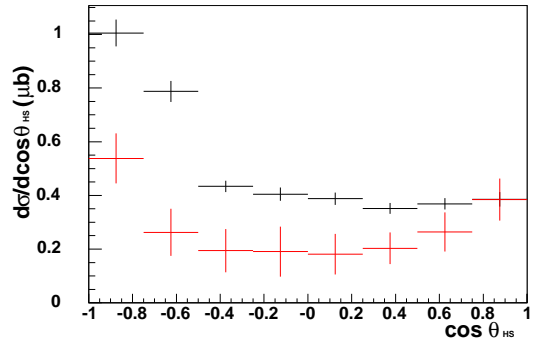
Fig. 19. An example of a (acceptance corrected) $\cos\theta_{HS}$ distribution before (black points) and after (red) the non-resonant $\pi^+\pi^-$ background subtraction ($0.58 < x_B < 0.64$ and $4.10 < Q^2 < 4.60$ GeV^2 bin). In this example the error bars are purely statistical and no systematic uncertainty has been added. The asymmetry in the red data points between $\cos\theta_{HS}=-1$ and $\cos\theta_{HS}=1$ is attributed to some remaining non-resonant $\pi^+\pi^-$ background which could not be subtracted by our fitting procedure, estimated to lead to a 25% systematic uncertainty (see section 2.4).

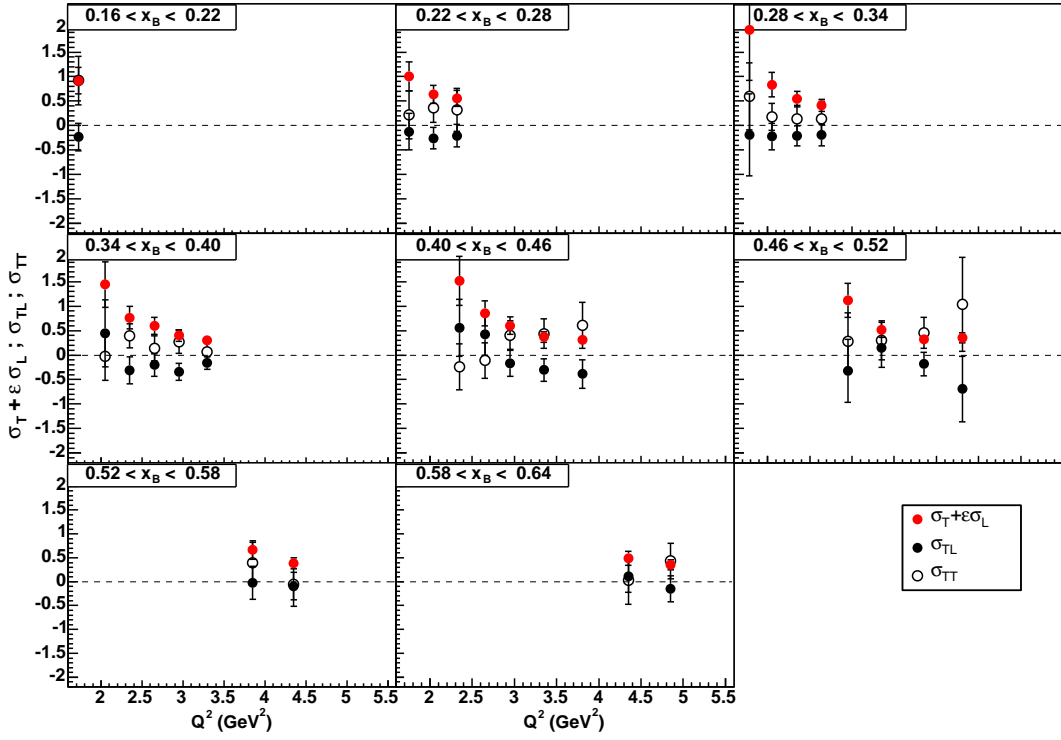**Fig. 17.** Cross sections $\sigma_T + \epsilon\sigma_L$, σ_{TT} and σ_{TL} (in μb) for the reaction $\gamma^*p \to p\rho^0$ as a function of Q^2 for different bins in x_B.

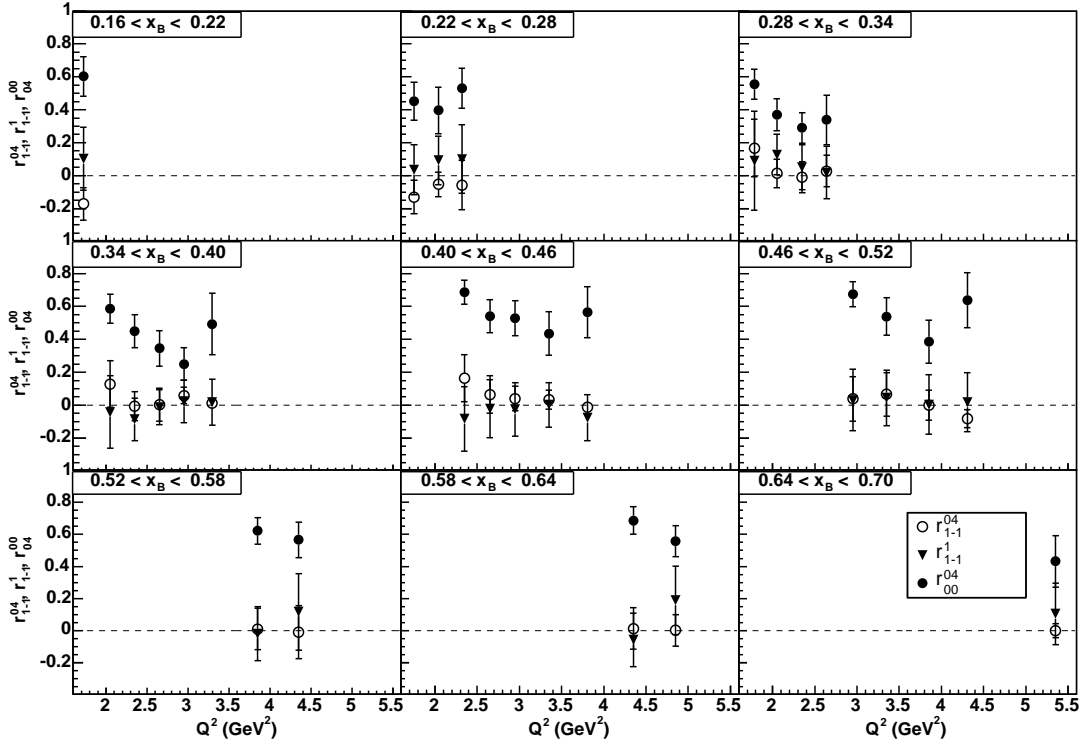**Fig. 18.** Density matrix elements r^{04}_{1-1}, r^1_{1-1} and r^{04}_{00} for the reaction $\gamma^*p \to p\rho^0$ as a function of Q^2 for different bins in x_B.
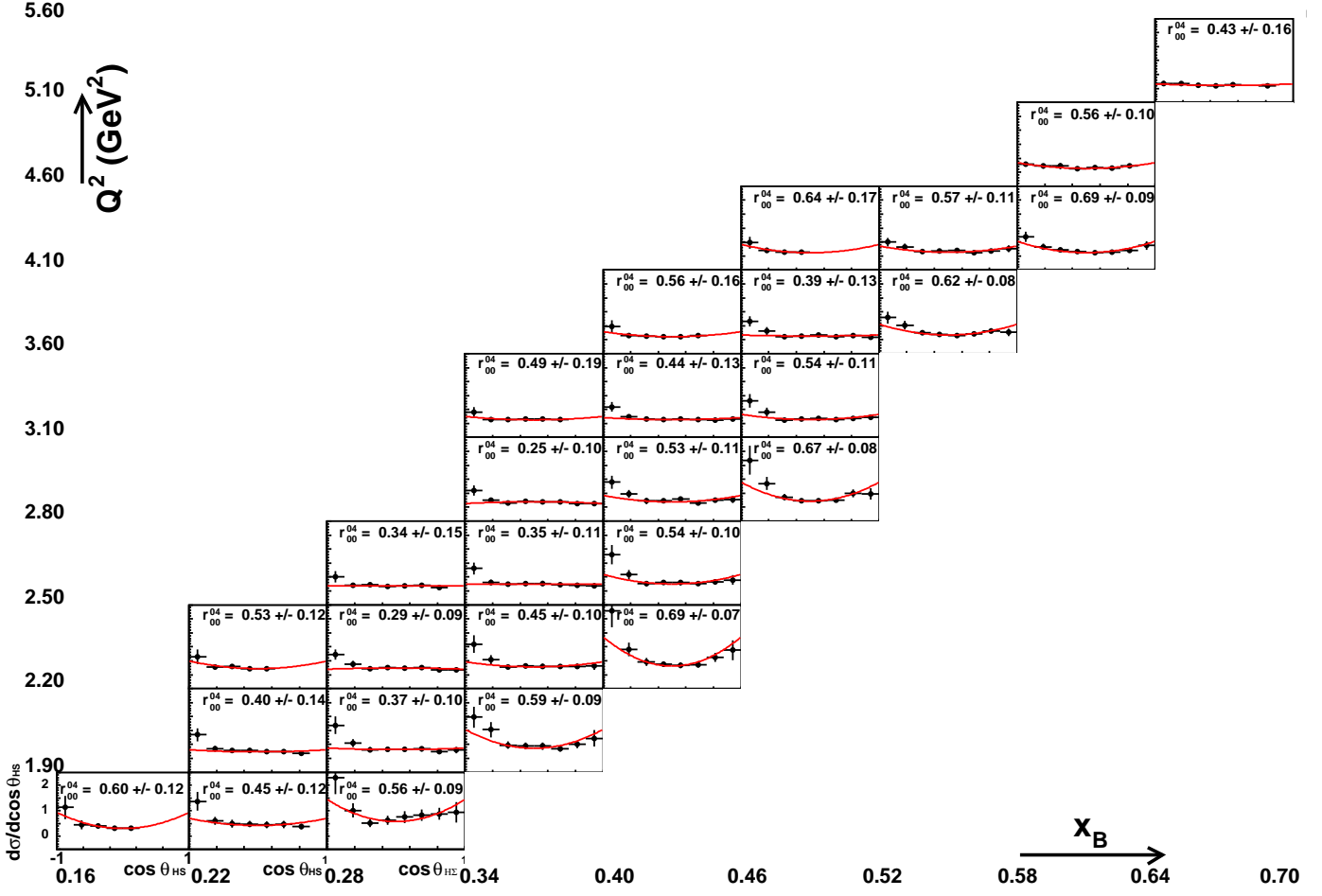
Fig. 20. Cross section $d\sigma/d\cos(\theta_{HS})$ (in μb) for all bins in (Q^2, x_B). The red curve corresponds to the fit with function 16.

2.7 Longitudinal/transverse cross section separation

Following the relative verification of the presence of SCHC in the previous discussion, the ratio R_ρ can be determined from:

$$R_\rho = \frac{\sigma_L}{\sigma_T} = \frac{1}{\epsilon}\frac{r_{00}^{04}}{1 - r_{00}^{04}}. \tag{17}$$

Although we cannot claim that our data give strong evidence for SCHC (nor for its violation), it should be noted that ref. [41] mentions that eq. 17 is relatively robust to violations of SCHC. Fig. 21 shows R_ρ for all our (Q^2, x_B) bins, assuming SCHC, which is an assumption that we will keep for the remainder of this analysis.

We fit our 27 points to a linear function:

$$R_\rho = a + bQ^2, \tag{18}$$

which yields: $a = 0.281 \pm 0.549$ and $b = 0.439 \pm 0.203$. The uncertainties on a and b are relatively large but highly correlated. The normalized correlation coefficent is 0.966. Fig. 22 shows that the band corresponding to our fit is in good agreement with the world's data.

The separated longitudinal and transverse cross sections, σ_L and σ_T, are then calculated as:

$$\sigma_T = \frac{\sigma_\rho}{(1 + \epsilon R_\rho)},\ \sigma_L = \frac{\sigma_\rho R_\rho}{(1 + \epsilon R_\rho)}. \tag{19}$$

We will display these resulting cross sections in section 3, where they will be compared to the theoretical models.

2.8 Systematic uncertainties

There are several sources of systematic uncertainties. The main one stems undeniably from the fit to extract the ρ^0 cross section and subtract the non-resonant $\pi^+\pi^-$ continuum, as discussed in section 2.4, and estimated to be 25%. We recall that this estimation arises from several analyses:

– Fitting the $M_{\pi^+\pi^-}$ distributions of fig. 11 and changing the shapes of the various inputs and contributions. Other systematic studies on these fits were carried out: removing a few data points on the edges of the $M_{\pi^+\pi^-}$ spectra to study edge effects, smoothing the histograms to take into account potential statistical fluctuations, varying the ranges of the parameters to
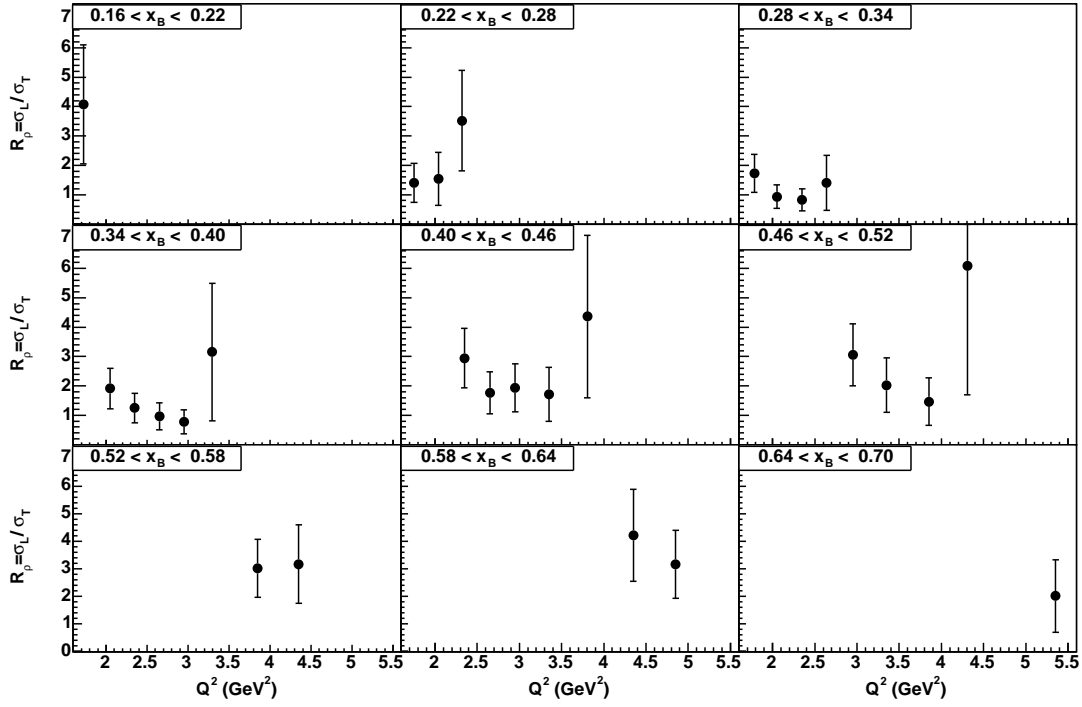
Fig. 21. The ratio R_ρ for the reaction $(\gamma^* p \to p\rho^0)$ as a function of Q^2 for different bins in x_B.
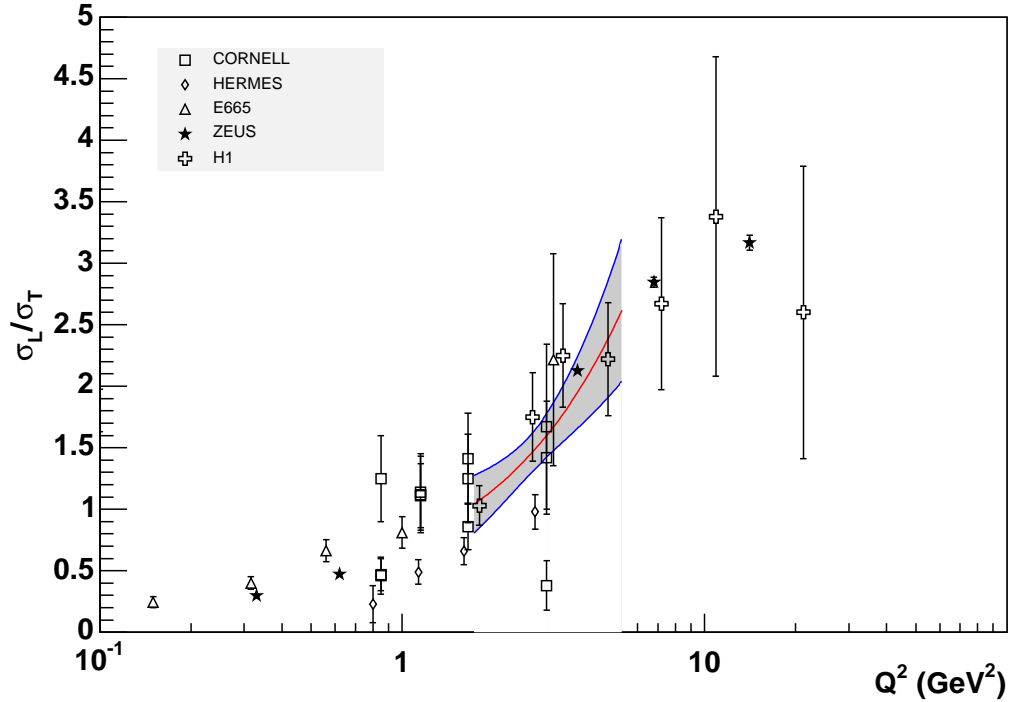
Fig. 22. World's data for R_ρ. The grey band represents the fit to eq. 18 using our 27 R_ρ points in (Q^2, x_B). The red line shows the central value of the fit while the blue lines show the associated uncertainty limits. The CORNELL, HERMES, E665, H1 and ZEUS data are respectively from refs. [19], [20], [33], [38] and [39].

be fitted (see Table 2), etc. All in all, we found a stability and robustness of our fits at the $\approx 20\%$ level.

– Integrating $d\sigma/dt$ over t (section 2.6) and comparing it to the total cross sections (section 2.5), resulting in a $\approx 20\%$ level agreement.

– Observing an asymmetry at the $\approx 25\%$ level between the forward and backward angles in the $\cos\theta_{HS}$ distributions (section 2.6).

A second source of systematic uncertainty stems from the acceptance calculation which is largely model independent. We have carried out several tests to determine the associated uncertainty on our procedure. For instance, we have varied the binning of the 7-dimensional table (see table 1). As an other test, we have also varied the input event generators: taking for instance only the $ep \rightarrow e'p\pi^+\pi^-$ phase space channel or only the $ep \rightarrow e'p\rho^0$ channel. Ultimately, we estimated the stability of our acceptance to be at the 15% level.

We correct the data for radiative effects. These were generated according to ref. [25]. The approximations used in this calculation may lead to systematic uncertainties that we estimate to be of the order of 4%.

The determination of the CC efficiencies relies on the assumption that the distribution of photoelectrons for detected electrons is a generalized Poisson function and that the shape of this distribution above 4 photoelectrons is sufficient to determine the whole distribution and to extrapolate to 0. The maximum error we could make on the integral of the distribution between 0 and 4 photoelectrons is about 25%. Since the CC inefficiencies are at most of the order of 6%, the corresponding systematic uncertainties on the cross sections is 1.5%.

The EC efficiency determination relies on the assumption that a particle with a sufficiently high number of photoelectrons in the CC was unambiguously an electron. We tried applying several values for this cut to estimate the stability of the results and the maximum differences were found to be on the order of 2%.

The target length is known to about $\pm$ 1 mm. The hydrogen density was kept fairly constant through temperature and pressure stabilization. The determination of the beam integrated charge also has a small systematic uncertainty. All this is summarized in table 3, and leads to a normalization error applicable to the whole data set.

Source of error	Estimated uncertainty
Fitting procedure	25%
CLAS acceptance	15%
Radiative corrections	4%
CC efficiency	1.5%
EC efficiency	2%
Target thickness	2%
Target density	1%
Beam integrated charge	2%

Table 3. Systematic uncertainties affecting the overall normalization. The quadratic sum of all theses errors results in a $\approx 30\%$ systematic error bar.
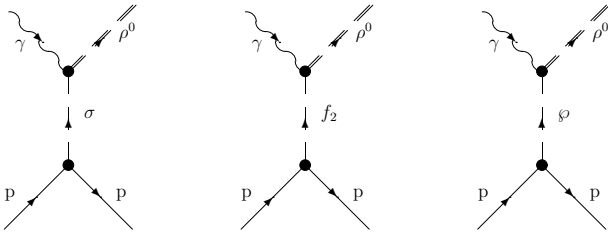
3 Theoretical interpretation

3.1 The Regge "hadronic" approach

The Regge approach consists of understanding exclusive ρ^0 electroproduction, above the resonance region and at forward angles where the cross section is the largest, in terms of exchanges of meson "trajectories" in the t-channel. Regge theory generalizes the notion of a t-channel *single* particle exchange to the notion of a *family* (i.e. trajectory) of particle exchanges. Indeed, mesons, and more broadly hadrons, appear in general in sequences made of rotational excitations. Mesons that have the same quantum numbers, except for spin, seem to align along linear "trajectories" $\alpha(t) = \alpha(0) + \alpha' t$ that relate their squared mass $-t$ to their spin α. This leads in the high energy limit to amplitudes proportional to $s^{\alpha(t)}$, where $s = W^2$, and therefore total cross sections are proportional to $s^{\alpha(0)-1}$.

In the following, we will use "JML" to refer to the latest version [42] of the model developed by J.-M. Laget and collaborators [11,12,43]. The dominant amplitudes correspond to the t-channel exchange diagrams of fig. 23. Since vector mesons have the same quantum numbers as the photon, systems with quantum numbers of the vacuum can be exchanged. The corresponding trajectory is called the pomeron. Although the pomeron contribution fully explains ϕ meson photo- [44] and electroproduction [45], it represents only about one third of the cross section in the $\gamma^*p \rightarrow p\rho^0$ channel for the energy range covered by our data. Here the bulk of the cross section comes from the exchange of the $f_2(1270)$ and σ mesons. The exchange of the π meson, which dominates ω production, contributes very little to the ρ^0 production channel.

Amplitudes for the pomeron, π and f_2 meson exchange diagrams can be found in ref. [11] and for the σ meson exchange diagram in ref. [43]. In photoproduction, the only parameters of the model are the coupling constants at the vertices of the diagrams. They are taken from a comprehensive study of other independent processes. For instance, the quark-pomeron coupling constant is fixed by the analysis of pp scattering at high energy ($W \sim 100$ GeV). In electroproduction, a monopole form factor is introduced at the $\gamma\pi\rho$ vertex and a dipole from factor is used at the $\gamma\sigma\rho$ vertex [11]. In this latter reference, a dependence on t is given to the cut-off mass that accounts for an increasing point-like behavior of the coupling of the photon with the meson when $-t$ (and consequently the impact parameter) increases. By construction, both the Q^2 and the t dependency of the $\gamma\wp\rho$ (where $\wp$ stands for the pomeron) and the $\gamma f_2\rho$ vertices are intrinsically part of the corresponding amplitudes, and no other parameters are included.

With this limited number of parameters, the JML model is able to successfully reproduce the main trends of the W and t dependences of the total and differential cross sections for the reactions $\gamma^*p \rightarrow p\phi$, $\gamma^*p \rightarrow p\omega$ and $\gamma^*p \rightarrow p\rho^0$ over the whole W range, i.e. from threshold up to HERA energies. In order to save computation, in our case, the pomeron exchange version of the model has been used

Fig. 23. Dominant t-channel exchange diagrams for the reactions $\gamma p \to p \rho^0$.

Fig. 24. The handbag diagrams for (longitudinal) vector meson production. Quark GPDs are accessed on the left and gluon GPDs are accessed on the right.

instead of the two gluon exchange version. In the momentum transfer range of this work, i.e. $-t < 2$ GeV^2, the two models lead to almost identical results. Overall, as was mentioned before, the pomeron/two-gluon exchange contribution does not dominate the cross section in the energy range that is accessed in this study (W up to 2.5 GeV).

3.2 The GPD "partonic" approach

The JML model was originally built for photoproduction, i.e. $Q^2 = 0$, and was extended to electroproduction by introducing form factors to take into account the shorter distances probed by the virtual photon, inversely related to Q^2. We now consider another approach, based on the formalism of Generalized Parton Distributions (GPDs), which is valid in the so-called Bjorken (or "Deep Inelastic") regime, i.e. $Q^2, \nu \to \infty$ with $x_B = \frac{Q^2}{2M\nu}$ finite. An important question is how low in Q^2 this asymptotic formalism can still be applied or extrapolated?

Collins *et al.* [7] have shown that the dominant processes for exclusive meson electroproduction, in the Bjorken regime, are given by the so-called handbag diagrams represented in fig. 24.

The handbag diagrams are based on the notion of factorization in leading-order pQCD between a hard scattering process, exactly calculable in pQCD and a nonperturbative nucleon structure part that is parametrized by the Generalized Parton Distributions introduced by Müller *et al.* [4], Ji [5] and Radyushkin [6]. For the quark handbag diagram and for vector mesons, only the two unpolarized GPDs contribute. They are called, using Ji's notation, H and E, and they depend upon three variables: x, ξ and t. We refer to the rich literature on GPDs (see refs. [8,9,10] for recent reviews) for the full definition of the formalism and of the variables. For the gluon handbag diagram, the
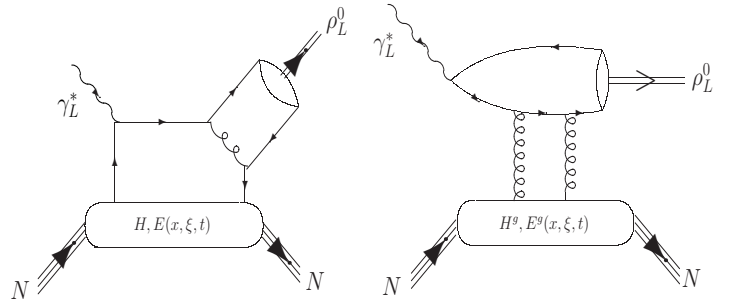
corresponding H^g and E^g gluonic GPDs are usually approximated by and reduced to the forward gluon density $G(x)$.

We recall that for mesons, factorization, which is an essential component of the handbag mechanism, is only valid for the longitudinal part of the cross section, as the L subscripts on the photon γ_L^* and on the meson ρ^0 indicate in fig. 24. This is one of the main motivations for separating the longitudinal and transverse parts of the cross sections in our data analysis.

We stress that theoretical calculations of exclusive meson production cross sections in the QCD factorization and GPD approaches are extremely challenging because one needs to address several issues at once: how to model the GPDs; how to treat the hard scattering process (the choice of an effective scale in α_s, the role of QCD corrections, etc.); how to consistently combine contributions from meson production in small-size and large-size configurations, etc. While in theory these are distinct issues that can be discussed separately, in practice they are very much related. Therefore, the choices and approximations one makes in the treatment of one will generally influence the conclusions one draws about the others.

In the following, we will discuss the two particular GK [13] and VGG [14,15,16,17] GPD-based calculations that provide quantitative results for the *longitudinal* exclusive ρ^0 cross section. Both groups have adopted the same approach. They parametrize the (x, ξ) dependence of the H and E GPDs based on double distributions as proposed in ref. [46], (the treatment of the t dependence being different). They correct the leading order amplitude with an intrinsic transverse momentum dependence, the so-called $k_\perp$ corrections or, more generally, the modified perturbative approach [47]. On this latter point, it is indeed well-known that at high W the leading-twist calculations overestimate the data and that the associated pre-

diction of $\frac{d\sigma_L}{dt}$ evolving as $\frac{1}{Q^6}$, at fixed x_B, is not observed in the data (see for instance ref. [48]).

The main difference between the two calculations lies in the fact that the GK group has treated the sum of the two handbags at the *amplitude* level, while the VGG group has treated it at the *cross section* level, and has therefore neglected the interference between the two handbag diagrams. We will see this effect in the next section where we compare our data to the two particular GPD models we have just introduced.

3.3 Comparison to data

Fig. 25 shows our results for the total *longitudinal* cross section for exclusive ρ^0 electroproduction on the proton as a function of W, for different Q^2 bins, along with the relevant world's data.

The cross sections clearly exhibit two different behaviors as a function of W. At low W the cross sections decrease with W and then begin to rise slowly at $W \approx 10$ GeV.

In fig. 25 the results of the calculations of the JML, VGG and GK models are also shown. The JML model (dash-dotted line) reproduces fairly well the two general behaviors just mentioned. The drop of the cross section at low W is due to the t-channel σ and f_2 meson exchange diagrams (see fig. 23). The intercept $\alpha(0)$ of the f_2 trajectory is ≈ 0.5 and therefore the cross sections decrease with energy as $\frac{1}{s^{0.5}}$. The flattening of the cross section near W $\approx$ 10 GeV comes from the combined effect of the decreasing f_2 contribution and the increasing pomeron contribution, whose trajectory has an intercept of $\alpha(0) \approx 1+\epsilon$. Although the JML model reproduces the general W dependence of the *longitudinal* exclusive ρ^0 cross section relatively well, it drops as a function of Q^2 faster than the data and agrees only up to $Q^2 \approx 4.10$ GeV^2.

We now turn to the GPD approaches. The dashed line shows the result of the GK model, while the thin solid line shows the result of the VGG model. We see that they give a good description of the high and intermediate W region, down to $W \approx 5$ GeV. This result was already observed by the HERMES collaboration [20]. At high W the slow rise of the cross section is due to the gluon and sea contributions, while the valence quarks contribute only at small W (this decomposition is shown in fig. 28 when we discuss the transverse cross section). We see a significant disagreement between the GK and VGG models at intermediate W, which can be clearly explained by the fact that, as was mentioned in section 3.2, the GK model takes the interference between the two handbag diagrams of fig. 24 into account, while the VGG model sums them *incoherently*. This interference is of course maximal at intermediate W's where the gluon handbag diagram starts to become significant, while the valence part of the quark handbag diagram is still significant. The data don't particularly favor GK over VGG but it is clear that, on purely theoretical grounds, the GK model is more correct. It is remarkable that, except in this intermediate W region, i.e.

in the high- and low-W regions, the GK and VGG models are in close agreement. The fact that two independent groups with different numerical methods and approximations tend to agree gives some relative confidence in the calculations.

At lower W values, where the new CLAS data lie, it is striking that both the GK and VGG models fail to reproduce the data. This discrepancy can reach an order of magnitude at the lowest W values. The trend of these particular GPD calculations is to decrease as W decreases, whereas the data increase. In the VGG and GK calculations, these trends can be understood as follows: GPDs are approximately proportional to the forward quark densities $q(x)$. This relation is not so direct since the quark densities are, in the double distributions ansatz of ref. [46], convoluted with a meson distribution amplitude but, still, the main trends remain. Then, as x increases (i.e. W decreases), GPDs tend to go to 0 since $q(x) \approx (1-x)^3$ for x close to 1. There might be, according to the scale, a slight local increase or bump around $x \approx 0.3$, due to the valence contribution, which is indeed clearly apparent in the VGG calculation shown in fig. 25. However, this variation cannot explain an increase of an order of magnitude.

The conclusion on the GPD approach is then two-fold:

– The handbag is not at all the dominant mechanism in the low W valence region and higher twists or so far uncontrollable non-perturbative effects obscure the handbag mechanism. If so, one has to explain why the (power-corrected) handbag mechanism works in the high/intermediate W (i.e. low x) domain and, quite abruptly, fails in the valence region. Higher twist can certainly depend on energy, but such a strong variation with W is certainly puzzling. Also, the explanation might simply be of a *kinematic* nature. As shown in fig. 14, the minimum value of $|t|$ increases significantly with decreasing W. For instance, $t_{min} \approx 1.6$ GeV^2 for the $(0.64 < x_B < 0.70, 5.10 < Q^2 < 5.60$ GeV$^2)$ bin while $t_{min} \approx 0.1$ GeV^2 for the $(0.16 < x_B < 0.22, 1.60 < Q^2 < 1.90$ GeV$^2)$ bin. In the handbag formalism, higher twists grow with t and this purely kinematic effect provides a natural source for them. However, more than absolute values, the ratio $\frac{t}{Q^2}$ should be relevant, and for the largest t_{min} values, one actually finds $\frac{t_{min}}{Q^2} = \frac{1.6}{5.35}$, i.e. of the order of 30%. More generally, the largest t_{min} values correspond to the largest Q^2 values but, since Q^2 increases faster than t_{min} in our kinematics, this actually makes the ratio $\frac{t}{Q^2}$ more favorable as Q^2 increases.

– Or the handbag mechanism, which succesfully describes the region of intermediate and high W, is indeed at work in the valence region but the way the GPDs are modeled by the VGG and GK groups is incomplete, with a significant and fundamental contribution missing, or incorrect.

Let us note at this stage that, on general grounds, at large x_B, the situation is somewhat more complex than at small x_B. Both real and imaginary parts contribute (the so-called ERBL and DGLAP regions), the skewness of the
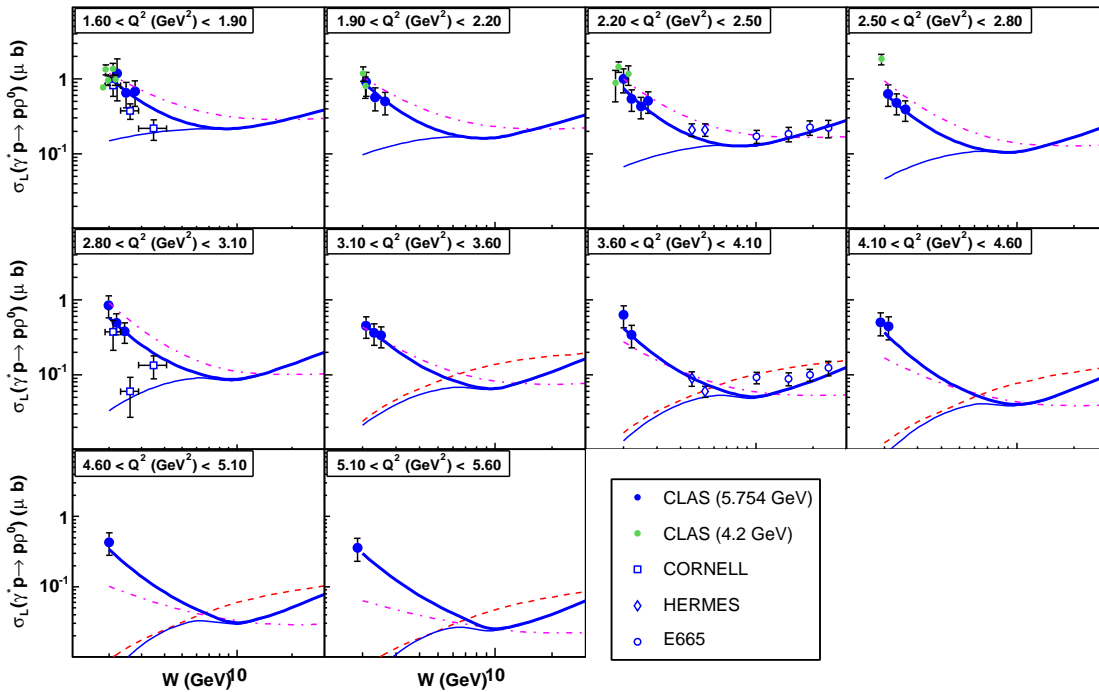
Fig. 25. World data for the reduced cross sections $\gamma_L^* p \to p\rho_L^0$ as a function of W for constant Q^2 bins, in units of μbarn. The lowest cross section point in the 2.80 GeV$^2 < Q^2 < 3.10$ GeV^2 bin (from CORNELL) corresponds to the low R_ρ (=0.38) point in fig. 22 and might be unreliable. The dashed curve shows the result of the GK calculation and the thin solid curve shows the result of the VGG calculation. Both calculations are based on Double Distributions as proposed in ref. [46] for the GPD parametrizations and incorporate higher twist effects through $k_\perp$ dependence. They differ essentially in summing coherently or not the gluon and the quark exchange handbag contributions (see fig. 24). The thick solid curve is the VGG calculation with the addition of the D-term inspired contribution. The dot-dashed curve shows the results of the Regge JML calculation. The 4.2 GeV CLAS, CORNELL, HERMES and E665 data are respectively from refs. [21], [19], [20] and [33].

GPDs is substantial and non-perturbative effects are expected to play a strong role in determining the behavior of the GPDs near $x \to \xi$. Therefore, it is not so clear whether the higher twist corrections, which are already substantial at low x_B through the $k_\perp$ dependence, have the same character at large x_B and if much can be concluded about large x_B from the good GPD description of the small x_B data.

Therefore, with utmost caution, we quote the suggestion of ref. [49] to add a new (strong) component to the standard VGG GPD parametrization, in the form of a D-term inspired ansatz, to reconcile the handbag approach with the data. We recall that the D-term was originally introduced by Polyakov and Weiss [50] in order to complete the Double Distribution representation of GPDs, so as to satisfy the polynomiality rule, and that it could be interpreted as the contribution to the GPDs of the exchange of a σ meson in the t-channel. In ref. [49], the t-dependence of the D-term was modified (making it, effectively, no longer a D-term, properly speaking) and renormalized. One of the motivations for this new term was to extend the concept of $q\bar{q}$ components, or t-channel meson exchange, in GPDs, in a spirit similar to the JML model that explains

the strong rise of the cross section as W decreases by t-channel σ and f_2 meson exchange processes. The thick solid line of fig. 25 shows the result of the introduction of this new contribution, added coherently to the standard VGG double distribution parametrization, with its normalization adjusted to the data.

We insist that this extra contribution is a speculation, which however does have the merit of providing numerical estimates of the cross section. Several alternative explanations should also be in order. GPDs can obviously be parametrized differently than in VGG and in GK. It was shown for instance that the spectator model of Hwang and Müller with an overlap representation for the modeling of the GPDs [51] produces naturally an enhancement at large x compared to the VGG model that should produce quark exchange cross sections dropping with increasing W. Also, NLO QCD corrections might be more sizeable in this region (see ref. [52]). Let us finally mention that, in the framework of the VGG model, the Feynman mechanism (or overlap diagram, see ref. [15] for instance) was calculated but, although it has the right W dependence, since it is a real contribution that lives in the $|x| < \xi$ region and therefore dominates at large x_B, its numerical
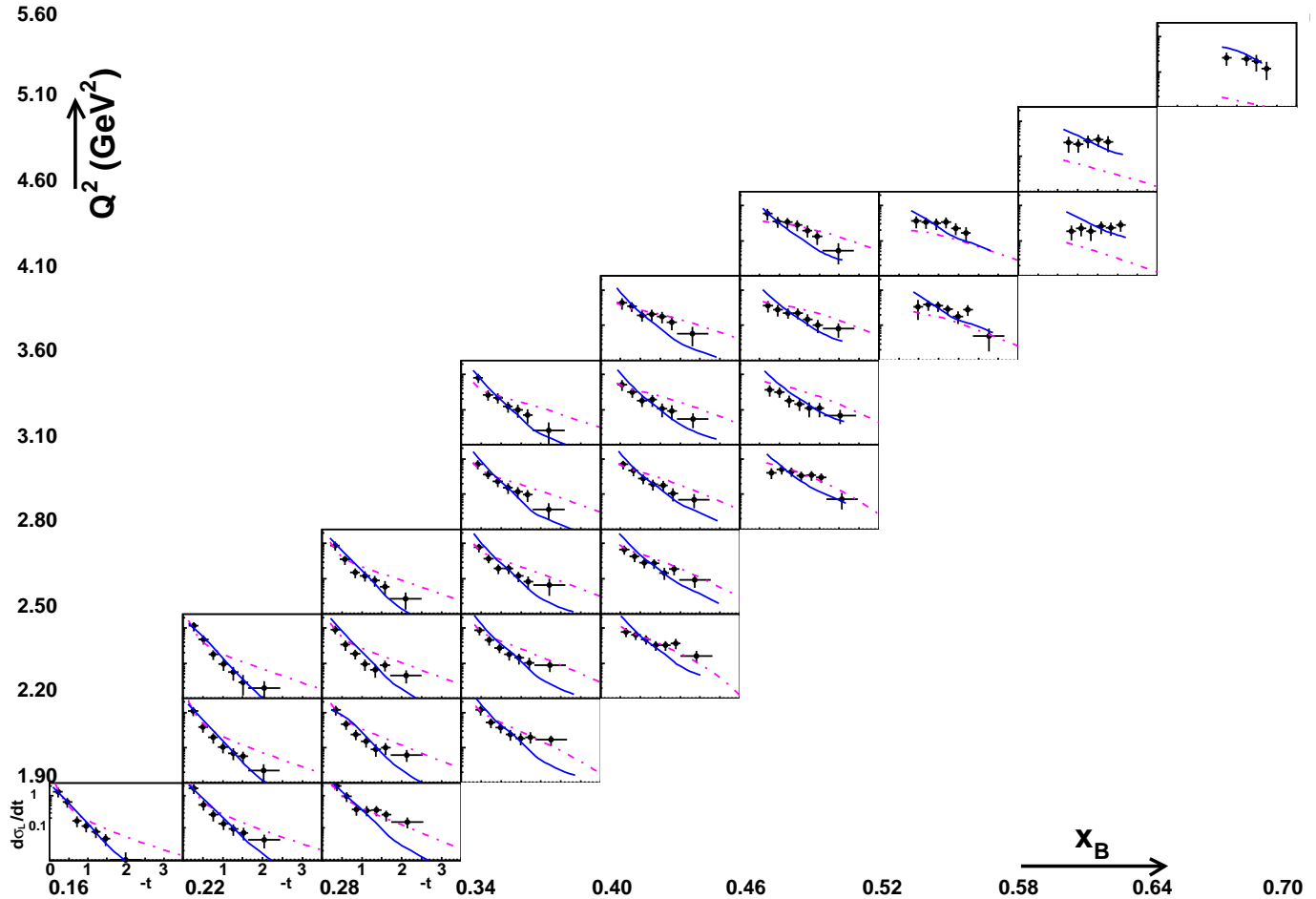
Fig. 26. Longitudinal cross section $d\sigma_L/dt$ (in $\mu b/GeV^2$) for all bins in (Q^2, x_B) as a function of t (in GeV^2). The thick solid curve represents the result of the VGG calculation with the addition of the Generalized D-term. The dash-dotted curve is the result of the JML model.

contribution, which does not rely on any extra parameter, is barely significant.

In summary, the only conclusion that we allow ourselves to reach at this stage is that the two popular GK and VGG models that provide numerical estimations of the $ep \rightarrow ep\rho^0$ cross sections and which describe well these data at large W values, fail to describe the present large x_B CLAS data (the normalisation as well as the W dependence). This fact does not imply however that the handbag mechanism is not at work in this latter regime as this might simply be an artifact of the current double distribution parametrization by these two groups. We reiterate that the necessary consistent treatment of GPD modeling, QCD scale setting, and higher-twist effects is much more difficult at low W than at high W and renders conclusions more difficult.

Fig. 26 shows the *longitudinal* differential cross section $d\sigma_L/dt$ as a function of t. The model of ref. [49], inspired partly by Regge theory, naturally explains the decrease of the t-slope as x_B gets larger. So does the spectator model of ref. [51], which quotes a decrease of the t slope from $b \approx 3.5$ GeV^2 at x_B=0.2 and Q^2=2 GeV^2 to $b \approx 1.5$ GeV^2 at x_B=0.6 and Q^2=5 GeV^2.

Let us mention here that because of the statistics of the data, which in general fall quite rapidly with t, we have not been able to extract reliably the ratio $R_\rho = \frac{\sigma_L}{\sigma_T}$ as a function of t and that, in a given (x_B, Q^2) bin, the *same* R_ρ value has been applied to the data over the whole t range. In other words, these differential cross sections might need to be corrected if the ratio R_ρ depends significantly on t.

The dash-dotted curves in fig. 26 show the JML model. In this approach, the natural t dependence given by the Regge formula $s^{\alpha(t)}$ is too sharp, as for the H and E GPD case. Thus, t-dependent form factors have to be introduced at the electromagnetic vertices of the diagrams of fig. 23, according to the procedure and motivations of ref. [42].

Fig. 27 shows the Q^2 dependence of the longitudinal ρ^0 cross section σ_L for different x_B values. When more than three points are present in an x_B bin, we fit the Q^2 dependence to the function $\frac{1}{Q^{2n}}$, with the extracted values n displayed in the figure. We recall that the handbag formalism predicts a value of 3 for n at asymptotically large Q^2 values. However, a smaller coefficient, i.e. a flatter Q^2 dependence, is expected at these low Q^2 values due to preasymptotic ($k_\perp$) effects. The thick solid (blue)
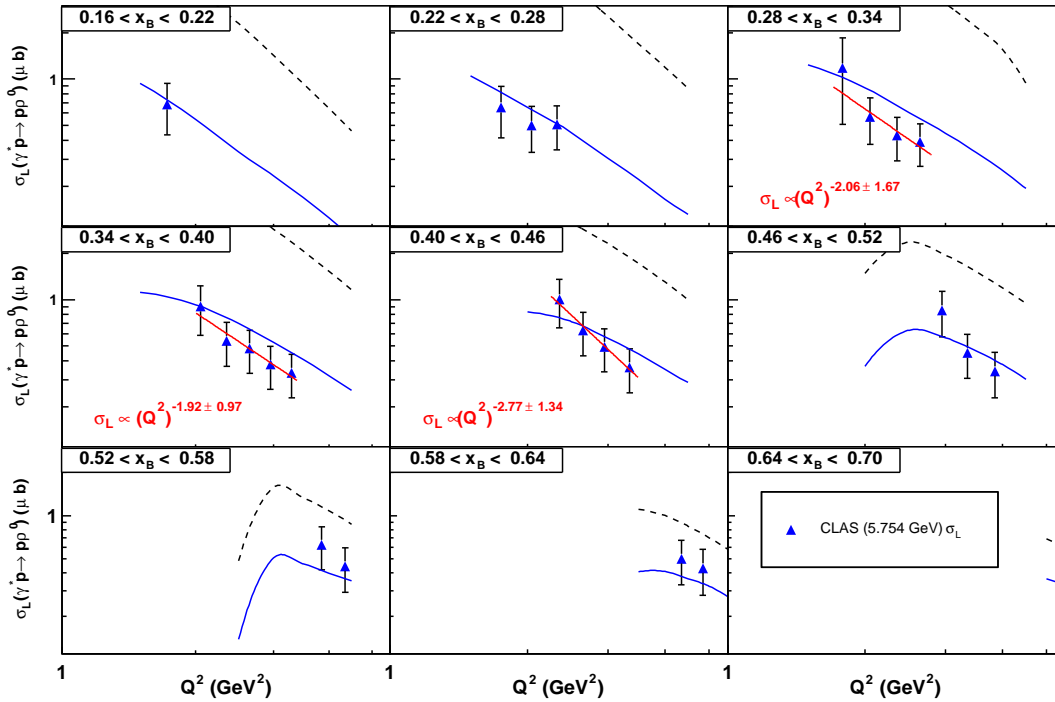
Fig. 27. Cross sections σ_L for the reaction $\gamma^* p \to p\rho^0$ as a function of Q^2 for different bins in x_B, in units of μbarn. The solid blue curve is the result of the VGG calculation with the Generalized D-term including the $k_\perp$ correction. The dashed curve shows the leading twist (i.e without the $k_\perp$ correction) VGG handbag calculation (with the Generalized D-term). The solid red curve is a fit to the data using a $\frac{1}{Q^{2n}}$ function.

curves in fig. 27 show the results of the VGG calculation including the extra aforementioned term. The magnitude and shape of the data are reasonably reproduced. The $k_\perp$ effects in the calculation flatten the Q^2 slope of the cross section. For comparison, the asymptotic result, i.e. without $k_\perp$ effects, is shown as the dashed (black) curve in fig. 27. One sees that its normalization is of course higher. Indeed, $k_\perp$ effects reduce the cross section by a factor 2 to 5 depending on x_B and Q^2. Also, the Q^2 dependence of the asymptotic result is steeper, precisely $\frac{1}{Q^6}$. At asymptotically large Q^2 values, the two calculations, i.e. with and without $k_\perp$ effects, are expected to agree.

To complete the interpretation of our data, we finally turn to the transverse part of the cross section. We show in fig. 28 the W dependence of the $\gamma_T^* p \to p\rho_T^0$ cross section for different Q^2 bins. The JML model (dot-dashed curve) once again reproduces the general shape of the W dependence of this cross section. Though, quantitatively, it seems to overestimate by $\approx 30\%$ the CLAS data at low Q^2, where it is expected to be the most valid. The agreement for the longitudinal part of the cross section was much better for this kinematical region.

The transverse part of the cross section doesn't lend itself straighforwardly to a GPD interpretation since it is higher twist. However, the GK group, taking into account $k_\perp$ effects, has been able to extend its analysis of

the longitudinal cross section to the transverse case [53]. They showed that retaining the quark transverse momenta regularizes the infrared singularities occuring in the transverse process. The dashed curve in fig. 28 shows the result of this calculation. The high energy E665 data, and to some extent, the HERMES data are well reproduced, thus comfirming the approach. However, as for the longitudinal cross section, the low W CLAS data are completely underestimated. The VGG model has not yet been extended to the transverse case but it is clearly expected that the addition of the Generalized D-term to the transverse process produces the same effect as for the longitudinal one and might explain the rise of the cross section at low W.

Finally, fig. 29 shows the transverse differential cross section $d\sigma_T/dt$ compared to the JML model. One finds that the JML model tends to overestimate the experimental cross sections at the $\approx 30\%$ level, especially at large t values.

4 Summary

Using the CLAS detector at JLab, we have collected the largest ever set of data for the $ep \to e'p\rho^0$ reaction in the valence region. We have presented the Q^2 and x_B (and W) dependences of the total, longitudinal and transverse

cross sections, as well as of the differential cross section in t.

The unique features that we have observed are:

– The W dependence of our data shows a clear decrease of the cross sections with increasing W, in contrast to the higher W data (HERMES, H1, ZEUS, E665), which show cross sections that tend to be flat or slowly rising with W,

– The t dependence exhibits a varying slope with energy: the slope increases as x_B decreases. In particular, our t dependences are almost flat at our largest x_B values,

– The cross sections decrease with Q^2 as approximatively $\frac{1}{Q^4}$, i.e. in a flatter way than what is predicted by the asymptotic handbag diagram.

These data and features can be interpreted in two ways:

– In terms of hadronic degrees of freedom, i.e. meson trajectory exchanges in the t-channel, following the JML Regge model. In order to reproduce the rather flat t dependences varying with Q^2 and x_B, electromagnetic form factors varying with Q^2 and t are necessary. For the longitudinal part of the cross section, good agreement with the data is found up to $Q^2 \approx 4.10$ GeV^2. For the transverse part of the cross section, there seems to be an overestimation (by $\approx 30\%$) of the cross section.

– In terms of partonic degrees of freedom, i.e. quark handbag diagrams and Generalized Parton Distributions. However, the GK and VGG calculations cannot provide the right W dependence of the cross section. This does not imply that GPDs cannot be accessed through exclusive ρ^0 electroproduction in the valence region but that possibly the way double distributions are modeled or the hard scattering amplitude is calculated in these two particular approaches should be modified or revisited. We stress that in exclusive meson electroproduction the GPD modeling problem is convoluted with other issues such as the treatment of the QCD scale setting, higher-twist effects, the meson distribution amplitude, etc. , rendering conclusions difficult. The present data will provide important input to improve our understanding of these fundamental QCD issues.

Acknowledgements

References

1. T. Regge, Nuovo Cimento, 14 (1959) 951; Nuovo Cimento, 18 (1960) 947.
2. P. D. B. Collins, "An introduction to Regge theory and high energy physics", Cambridge University Press, Cambridge (1977).
3. J. K. Storrow, Rep. Prog. Phys. 50 (1987) 1229.
4. D. Müller, D. Robaschik, B. Geyer, F.-M. Dittes, and J. Horejsi, Fortschr. Phys. **42** (1994) 101.
5. X. Ji, Phys. Rev. Lett. **78** (1997) 610; Phys. Rev. D **55** (1997) 7114.
6. A.V. Radyushkin, Phys. Lett. B **380** (1996) 417; Phys. Rev. D **56** (1997) 5524.
7. J.C. Collins, L. Frankfurt and M. Strikman, Phys. Rev. D **56** (1997) 2982.
8. K. Goeke, M. V. Polyakov and M. Vanderhaeghen, Prog. Part. Nucl. Phys. **47** (2001) 401.
9. M. Diehl, Phys. Rept. **388** (2003) 41.
10. A.V. Belitsky and A.V. Radyushkin, Phys. Rept. **418** (2005) 1.
11. J.-M. Laget, Phys. Lett. B **489** (2000) 313.
12. F. Cano and J.-M. Laget, Phys. Rev. D **65** (2002) 074022.
13. S. V. Goloskokov and P. Kroll, Eur. Phys. J. C **42** (2005) 281; Eur. Phys. J. C **50** (2007) 829.
14. M. Vanderhaeghen, P.A.M. Guichon, and M. Guidal, Phys. Rev. Lett. **80** (1998) 5064.
15. M. Vanderhaeghen, P.A.M. Guichon, and M. Guidal, Phys. Rev. D **60** (1999) 094017.
16. K. Goeke, M.V. Polyakov and M. Vanderhaeghen, Prog. Part. Nucl. Phys. **47** (2001) 401.
17. M. Guidal, M.V. Polyakov, A.V. Radyushkin and M. Vanderhaeghen, Phys. Rev. **D72** (2005) 054013.
18. P. Joos *et al.*, Nucl. Phys. B **113** (1976) 53.
19. D.G. Cassel *et al.*, Phys. Rev. D **24** (1981) 2787.
20. A. Airapetian *et al.*, Eur. Phys. J. C **17** (2000) 389.
21. C. Hadjidakis *et al.*, Phys. Lett. B **605** (2005) 256.
22. B. Mecking *et al.*, Nucl. Instrum. Meth. A **503** (2003) 513.
23. W.-M. Yao *et al.*, J. Phys. Lett. G **33** (2006) 1.
24. M. Battaglieri, R. Devita and M. Ripani, INFN Genova, private communication.
25. L.W. Mo and Y.S. Tsai, Rev. of Mod. Phys. **41** (1969) 205.
26. L.N. Hand, Phys. Rev. **129** (1963) 1834.
27. M. Ripani *et al.*, Phys. Rev. Lett. **91** (2003) 022002.
28. V. Mokeev *et al.*, Phys. Atom. Nucl. **64** (2001) 1292.
29. T.H. Bauer, R.D. Spital and D.R. Yennie, Rev. of Mod. Phys. **50** (1978) 261.
30. J.D. Jackson, Nuovo Cimento **34** (1964) 1644.
31. M. Ross and L. Stodolsky, Phys.Rev. **149**, (1966) 1172.
32. P. Söding, Phys. Lett. **19** (1966) 702.
33. M. R. Adams *et al.*, Z. Phys. C **74** (1997) 237.
34. M. Battaglieri and A. P. Szczepaniak, private communication.
35. L. A. Ahrens *et al.*, Phys.Rev.Lett. **42** (1979) 208.

36. P. Amaudruz *et al.*, Z. Phys. C **54** (1992) 239.

37. W. R. Francis *et al.*, Phys.Rev.Lett. **38** (1977) 633.

38. S. Aid, Nucl. Phys. B **468** (1996) 3, C. Adloff, Eur. Phys. J. C **13** (2000) 371.

39. J. Breitweg, Eur. Phys. J. C **6** (1999) 603.

40. K. Schilling and G. Wolf, Nucl. Phys. B **61** (1973) 381.

41. A. Ackerstaff *et al.*, Eur. Phys. J. C **18** (2000) 303.

42. J. M. Laget, Phys. Rev. D **70** (2004) 054023.

43. F. Cano and J. M. Laget, Phys. Lett. B **551** (2003) 317.

44. E. Anciant *et al.*, Phys. Rev. Lett. **85**, 4682 (2000).

45. J. P. Santoro *et al.*, arXiv:0803.1592 [nucl-ex].

46. A.V. Radyushkin, Phys. Rev. D **59** (1999) 014030; Phys. Lett. B **449** (1999) 81.

47. J. Botts and G. Sterman, Nucl. Phys. B **325** (1989) 62.

48. L. Frankfurt, W. Koepf and M. Strikman, Phys. Rev. D **54** (1996) 3194.

49. M. Guidal and S. Morrow, *Proceeding of the International Workshop "Exclusive reactions at high momentum transfer", Jefferson Laboratory, Newport-News, Virginia, USA, May 21-24 2007*, World Scientific, arXiv:0711.3743 (hep-ph).

50. M. Polyakov and C. Weiss, Phys. Rev. D **60** (1999) 114017.

51. D. S. Hwang and D. Müller, Phys. Lett. B **660** (2008) 350.

52. M. Diehl and W. Kugler, Phys. Lett. B **660** (2008) 202.

53. S. V. Goloskokov and P. Kroll, Eur. Phys. J. C **53** (2008) 367.
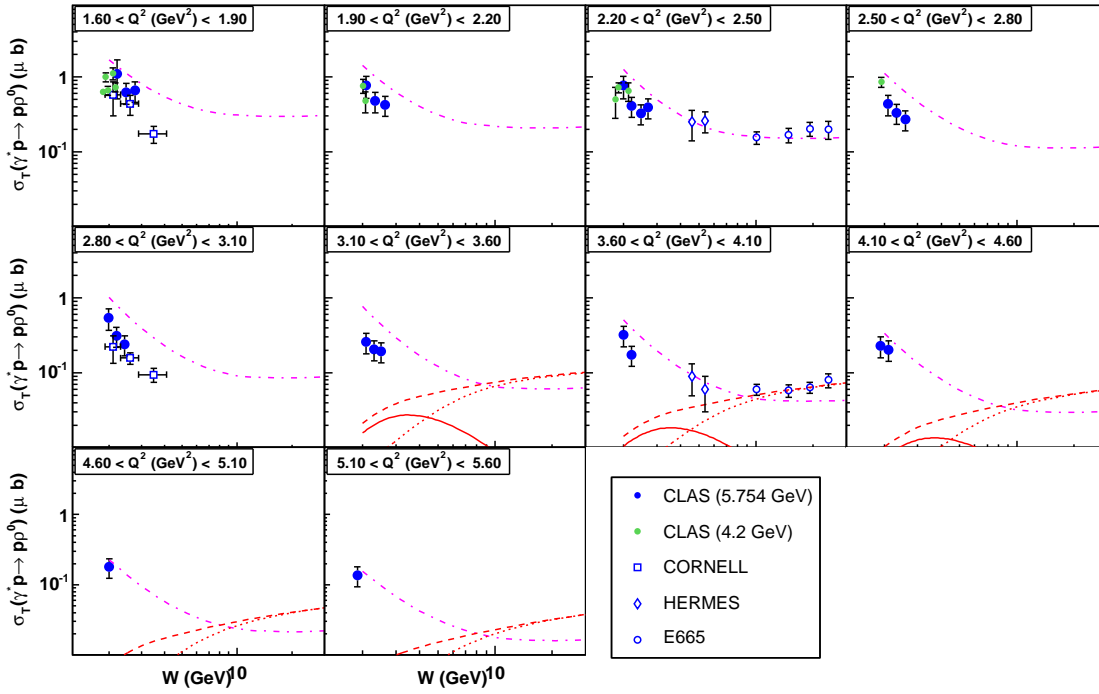
Fig. 28. World data for the reduced cross sections $\gamma_T^* p \to p\rho_T^0$ as a function of W for constant Q^2 bins, in units of μbarn. The dashed curve shows the result of the GK calculation. The solid curve shows the contribution of the valence part of the quark exchange handbag diagram (fig. 24 left) while the dotted curve shows the sum of the sea quarks part of the quark exchange handbag (fig. 24 left) and of the gluon exchange (fig. 24 right) contributions. The dot-dashed curve shows the results of the Regge JML calculation. The 4.2 GeV CLAS, CORNELL, HERMES and E665 data are respectively from refs. [21], [19], [20] and [33].
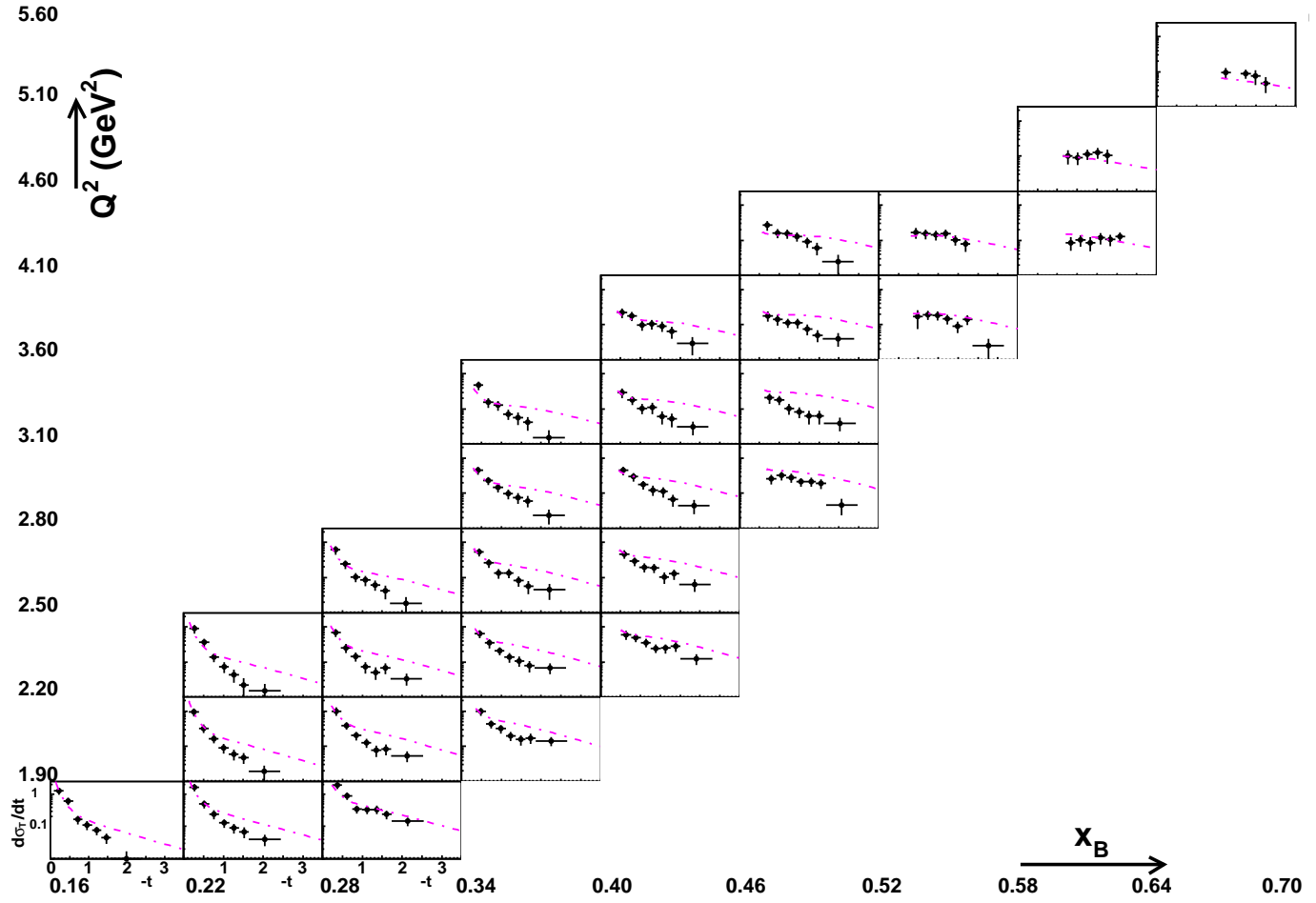
Fig. 29. Cross section $d\sigma_T/dt$ (in μb/GeV^2) for all bins in (Q^2, x_B) as a function of t (in GeV^2). The dash-dotted curve is the result of the JML model.